

Dynamic Rupture Models for the Southern San Andreas Fault

by Geoffrey P. Ely, Steven M. Day, and Jean-Bernard Minster

Abstract Dynamic rupture, and resultant ground motions up to 0.25 Hz, are simulated for an M_w 7.6 earthquake on the southern San Andreas fault. Spontaneous rupture is modeled with slip-weakening friction, and 3D viscoelastic wave solutions are computed with a support-operator numerical method. The initial traction model is derived from inversions of the M_w 7.3 1992 Landers strong ground-motion records, and borrows heavily from that used for the TeraShake2 simulations by [Olsen *et al.* \(2008\)](#). Heterogeneity in the traction model leads to focusing of the rupture front, and the focusing produces cases of supershear rupture velocity in asperities (areas of high initial traction), as well as cases of high peak slip rate and cohesive zone contraction in antiasperities. Separate solutions are computed for version 3.0 and 4.0, respectively, of the Southern California Earthquake Center Community Velocity Model (SCEC-CVM). We also compare the case of a flat ground surface (a common simplification made for finite-difference simulations) to the case of the ground surface conformed to regional topography. The overall distribution of simulated ground motion intensity is consistent with that derived from the empirical model of [Campbell and Bozorgnia \(2008\)](#), in the sense that the bulk of simulated pseudospectral velocity (PSV) values are within the 68% confidence intervals of the empirical model. Simulated PSVs corresponding to low probability in the empirical model are principally associated with basin wave-guide and directivity effects. An important example, first identified by the TeraShake1 simulations ([Olsen *et al.*, 2006](#)), is the stronger than expected ground motions at the site of Montebello due to a basin wave-guide effect. We find that this effect is lessened for version 4.0 of the SCEC-CVM, relative to version 3.0, due to a shallower model for the Chino basin.

Online Material: Visualizations of dynamic rupture and surface wave propagation.

Introduction

The southern San Andreas fault (SAF) is one of the most likely sources for the next large earthquake in southern California. The [Working Group on California Earthquake Probabilities \(1995\)](#) estimates the San Bernardino Mountain segment has a 28% probability of rupturing within 30 years, and the Coachella Valley segment has a 22% probability. A combined rupture of both segments, that study estimates, would produce an M_w 7.6 earthquake in close proximity to the greater Los Angeles area. The San Bernardino and Coachella segments last ruptured in 1812 and 1690 ± 20 , respectively ([Weldon *et al.*, 2004](#)), events that occurred well before the deployment of seismic networks in southern California. So in the absence of ground-motion records from a large SAF event in this region, we are faced with large uncertainty in the expected ground motion from a future event.

Large-scale numerical simulations by scientists such as [Frankel \(1993\)](#), [Graves \(1998\)](#), and Bielak (unpublished manuscript, 2009) have been used to help address some of this

uncertainty. The TeraShake1 simulations by [Olsen *et al.* \(2006\)](#) modeled 0–0.5 Hz motion from an M_w 7.7 event on the southern SAF, using kinematic source models. The kinematic sources were derived from slip models of the 2002 M_w 7.9 Denali earthquake by [Oglesby *et al.* \(2004\)](#). Wave fields were propagated through the Southern California Earthquake Center Community Velocity Model (SCEC-CVM) version 3.0 ([Magistrale *et al.*, 2000](#); [Kohler *et al.*, 2003](#)) with a staggered grid finite-difference method. For a northwest propagating rupture, they found unexpectedly large ground motion in the Los Angeles basin that they attribute to a wave-guide effect. The wave guide is formed by the continuous chain of basins, connecting the fault zone to the Los Angeles basin, lying at the southern foot of the San Gabriel and San Bernardino mountains. The assumption of constant rupture velocity in their kinematic model, however, may have overestimated rupture directivity effects. TeraShake1 was followed by the TeraShake2 simulations by [Olsen *et al.* \(2008\)](#)

that investigated similar scenarios, replacing the kinematic models with spontaneous rupture models. They found that the reduced coherency of the wave field due to source complexities in the dynamic model, that were not present in the kinematic TeraShake1 simulations, significantly reduced the predicted ground motion in Los Angeles. They considered multiple scenarios with different initial stress models, including both northwest and southeast propagating unilateral rupture. A two-step procedure was used in which the fault and velocity model were first conformed to rectangular mesh (as required by the staggered finite-difference method) for computation of the spontaneous rupture solution on a planar fault. The resultant slip motions were then mapped back to their proper spatial positions (on the original nonplanar fault model of the SAF) and used as kinematic source functions for the wave propagation simulation.

This article reexamines one of the northwest propagating TeraShake2 scenarios, with updated version 4.0 of the SCEC-CVM (Magistrale, 2005). Simulations are performed with the Support Operator Rupture Dynamics (SORD) code developed by Ely *et al.* (2008, 2009). SORD is based on a numerical scheme able to handle nonplanar boundaries, allowing rupture dynamics (on the nonplanar SAF model) and wave propagation to be computed simultaneously, and allowing ground-surface topography to be included in the simulations (as was not the case in the TeraShake models). We present a set of spontaneous rupture models that compare rupture behavior and ground motion using the two versions of the SCEC-CVM and also compare results from a flattened topography model with those from a model incorporating southern California topography and bathymetry at the free surface.

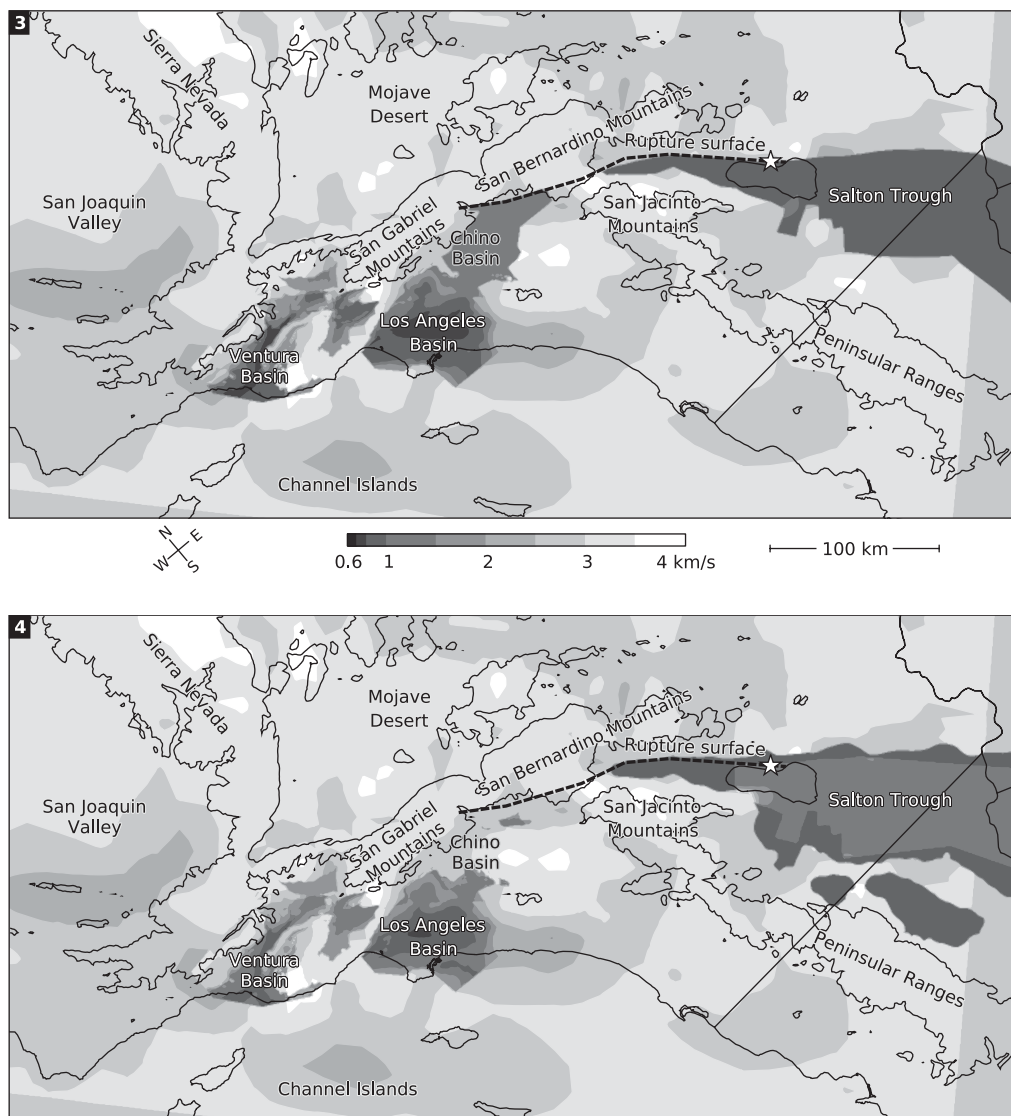


Figure 1. Model region maps, with topography contoured at 1 km elevation, and grayscale indicating S -wave velocity at 500 m depth for the SCEC-CVM version 3.0 (top) and version 4.0 (bottom). Version 4.0 incorporates a more complete Salton Trough model and a shallower Chino basin model.

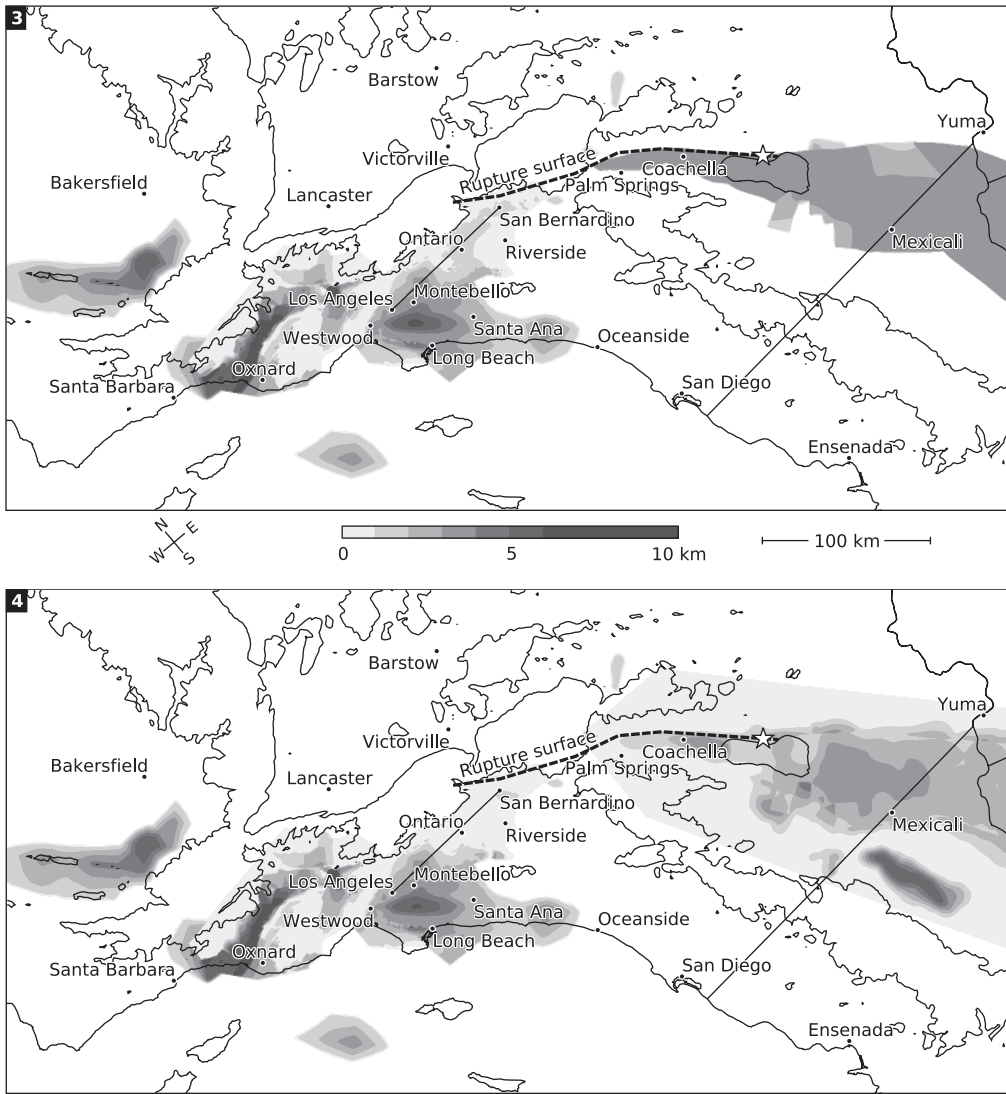


Figure 2. Sedimentary basin depth for the SCEC-CVM version 3.0 (top) and version 4.0 (bottom), as defined by the depth to the shallowest occurrence of *S*-wave velocities greater than 2.5 km/sec. Also shown are the vertical strike-slip rupture surface, the Los Angeles to San Bernardino cross section (Fig. 3), and the receiver locations.

Wave Propagation Model

The modeling region is a $600 \times 300 \times 80$ km volume that includes onshore and offshore southern California, as well as northernmost Baja California. The elastic properties of the volume are obtained from the SCEC-CVM, a 3D model of the upper mantle, crust, and sedimentary basins compiled from a broad range of sources, including surface geology, geotechnical borings, gravity, seismic refraction, regional and teleseismic tomography, and teleseismic receiver functions. The ocean water volume is treated as free space in our models. Version 4.0 of the SCEC-CVM (Magistrale, 2005) updates version 3.0 with a more complete description of the Salton Trough (Fig. 1) and shallower depth-to-basement rock in the Chino basin based on gravity and seismic reflection data (Figs. 2, 3).

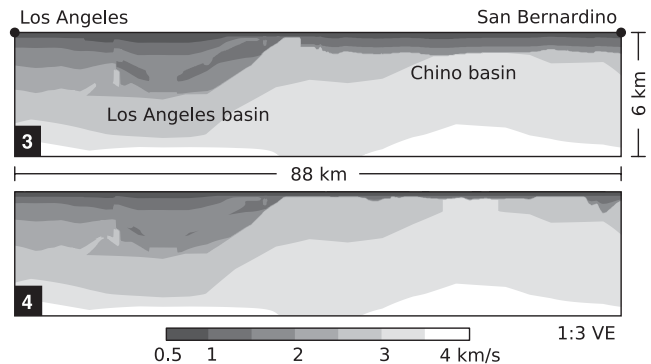


Figure 3. Cross section of *S*-wave velocity from Los Angeles to San Bernardino for SCEC-CVM version 3.0 (top) and version 4.0 (bottom). The Chino basin at this location is 1 km deep in version 3.0, and 400 m deep in version 4.0.

Table 1

Comparative Summary of the Numerical Wave Simulation Methods Used for TeraShake Simulations by [Olsen et al. \(2008\)](#) and for the Support Operator Rupture Dynamics Code

	TeraShake	Support Operator Rupture Dynamics Code
Numerical scheme	Finite difference	Support operator
Operator accuracy	$O(\Delta x^4, \Delta t^2)$	$O(\Delta x^2, \Delta t^2)$
Points per wavelength requirement	≈ 5	≈ 10
Mesh	Uniform rectangular, staggered grid	Hexahedral, partially staggered grid
Attenuation model	Course grain memory $Q \sim V_S$	Kelvin-Voigt viscosity $Q \sim V_S \omega^{-1}$
Absorbing boundary	Perfectly matched layer	Perfectly matched layer

Wave solutions in the volume are computed with an explicit support-operator method ([Ely et al., 2008](#)). The method uses curved hexahedral meshes and is second-order accurate in space and time. The Kelvin-Voigt model of viscoelasticity is used, for which the anelastic quality factor Q is inversely proportional to wave frequency. Besides the anelastic energy losses (attenuation) provided by this model during wave propagation, the viscosity helps to prevent numerical noise from affecting the (nonlinear) rupture calculations. Numerical dispersion extends to lower frequencies in low-velocity material, so we make viscosity inversely proportional to the S-wave velocity by setting the dimensionless damping parameter γ to $400/V_S$. The γ parameter, perhaps misleadingly labeled viscosity by [Ely et al. \(2008, 2009\)](#), is equivalent to the $\bar{\eta}$ damping parameter of [Day et al. \(2005\)](#) scaled by the time step Δt .

In order to increase the resolvable bandwidth of the simulations, we set artificial lower limits of 500 m/sec for S-wave velocity, and 1500 m/sec for P-wave velocity. Assuming that 3% or less errors in phase velocities are acceptable, the 1D finite-difference dispersion relation for the elastic wave equation ([Hughes, 2000](#), for example) dictates at least eight points of resolution per S wavelength. For a minimum S velocity of 500 m/sec, this gives better than 3% phase velocity accuracy up to about 0.3 Hz. This was demonstrated by [Ely et al. \(2008\)](#) for the SOM method on problems with layered media, a planar free-surface boundary, and highly distorted elements. The canyon test in [Ely et al. \(2008\)](#), which is extreme topography and therefore is probably a conservative test, suggests that the points-per-wavelength criterion doubles in the presence of a free-surface topography. Assuming a minimum S velocity of 1000 m/sec in the areas of significant nonplanar topography (as is evident

from Fig. 1), this again gives acceptable accuracy up to about 0.3 Hz. To allow for the shorter wavelength of Rayleigh waves relative to S waves of the same frequency, as well as some additional conservatism, we analyze the results only in the 0–0.25 Hz band.

For comparison, the fourth-order finite-difference method of the TeraShake simulations, needing approximately five grid points per wavelength, is able to resolve up to 0.5 Hz, for the same grid spacing. Additionally, TeraShake incorporates a more realistic attenuation model using the coarse-grained memory variable technique ([Day, 1998](#); [Day and Bradley, 2001](#)). The memory variable technique can model attenuation that is nearly constant with respect to frequency, which is a good representation of crustal material within the simulation bandwidth. The higher order accuracy and more realistic attenuation model make the TeraShake method superior for modeling waves in rectangular geometries. The advantage of SORD and similar methods is in modeling nonplanar topography and fault surfaces. Both TeraShake and SORD suppress artificial boundary reflections with perfectly matched layers (PML), introduced by [Berenger \(1994, 1996\)](#), and adapted to their respective numerical schemes by [Marrinkovich and Olsen \(2003\)](#) and [Ely et al. \(2008\)](#). A summary of the relative merits of TeraShake and SORD is given in Table 1.

Source Model

The fault geometry (shown in map view, Fig. 1) is modeled by five planar segments vertically extrapolated from the SAF trace in the 2002 USGS National Hazard Maps by [Frankel et al. \(2002\)](#). The total length is 200 km, and the depth is 16 km. This simplified geometry facilitated the procedure

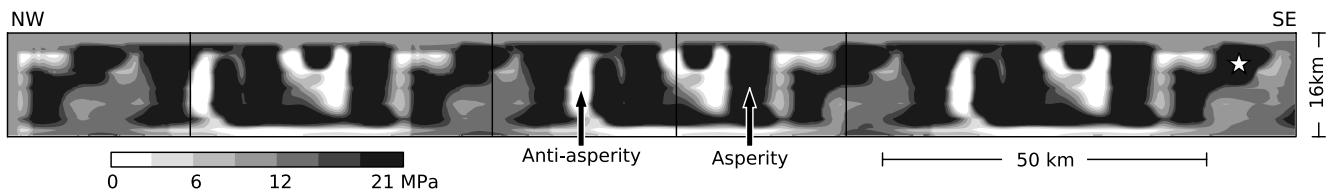


Figure 4. Initial shear traction on the fault surface based on dynamic inversion of strong motion records from the M_w 7.3 1992 Landers earthquake. To scale the Landers event up to the required fault length, the distribution is repeated multiple times laterally. Initial normal traction is constant over the fault at -20 MPa.

Table 2
Model Parameters

Model size	600 × 300 × 80 km
Simulation time	180 sec
Elements	3000 × 1500 × 400
Time steps	15,000
Δx Node spacing	≈200 m
Δt Time step	0.012 sec
V_p P-wave velocity	min: 1500 m/sec max: 8298 m/sec
V_s S-wave velocity	min: 500 m/sec max: 4849 m/sec
γ Viscous damping parameter	400/ V_s
τ_s^0 Initial shear traction	mean: 13.4 MPa max: 20.9 MPa
τ_n^0 Initial normal traction	-20 MPa
μ_s Coefficient of static friction	1.1
μ_d Coefficient of dynamic friction	0.5
d_0 Slip-weakening displacement	0.5 m

used in TeraShake2 to map the fault and surrounding velocity model to a rectangular grid. Though our numerical scheme does not have the same geometrical restrictions, we use identical fault geometry for consistency in comparing results. The largest misrepresentation of the simplified geometry, relative to known geology, lies in the constricting bend east of San Gorgonio Pass (at about the midpoint of the rupture trace), where the true fault dip is much less than 90° (Seeber and Armbruster, 1995) and, by geometrical considerations, the slip must have a thrust component.

Spontaneous rupture is modeled with a frictional boundary condition across the fault surface at which the frictional strength is determined by the negative product of the normal traction τ_n (negative in compression) and the coefficient of friction μ_f . The fault slips necessarily to ensure that shear traction never exceeds the frictional strength

$$|\tau_s| \leq -\mu_f \tau_n. \quad (1)$$

The model of friction is a slip-weakening law, with the coefficient of friction given by

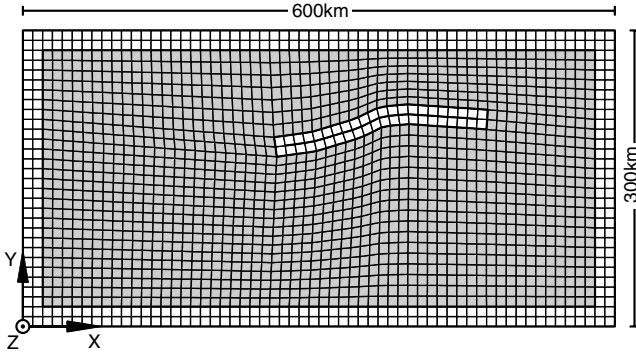


Figure 5. Map view, low resolution representation of the curved hexahedral mesh. Along the boundaries, within the PML zones, grid lines are orthogonal to the boundary. In elements surrounding the fault, grid lines are orthogonal to the fault surface. Elsewhere, within the elements shaded gray, grid lines are linearly interpolated.

Table 3
Model Statistics

		Model 3F	Model 4F	Model 4T
M_0	Moment (EN-m)	269.5	267.8	266.8
M_w	Moment magnitude	7.587	7.585	7.584
$\langle \Delta \tau_s \rangle$	Mean stress drop (MPa)	3.86	3.74	3.77
$\langle s \rangle$	Mean slip (m)	3.03	2.79	2.78
s_{max}	Maximum slip (m)	15.21	10.60	11.64
$\langle \dot{s}_{peak} \rangle$	Mean peak slip rate (m/sec)	3.21	2.86	2.84

$$\mu_f(\ell) = \begin{cases} \mu_s - (\mu_s - \mu_d)\ell/d_0 & \ell \leq d_0 \\ \mu_d & \ell > d_0, \end{cases} \quad (2)$$

where μ_s and μ_d are the coefficients of static and dynamic friction, ℓ is the slip-path length, and d_0 is the slip-weakening displacement. Further discussion of the fault boundary condition, including implementation of traction-at-split-node numerical solution method, is given by Day *et al.* (2005) and Ely *et al.* (2009).

To obtain a plausible set of dynamic parameters for the TeraShake2 scenarios, Olsen *et al.* (2008) used the results of a dynamic inversion of the M_w 7.3 1992 Landers earthquake by Peyrat *et al.* (2001) that achieved good fit to Landers near-field strong motion records in the 0–0.5 Hz band. For TeraShake2, the Landers inversion model was scaled up to an M_w 7.7 event by replicating the rupture three times laterally to extend it to the total length to 200 km. Strong ground motion provides fairly good constraint on the stress drop $\Delta\tau = |\tau_s^0| + \mu_d \tau_n$. It does not by itself, however, provide good constraint on the absolute magnitudes of τ_n , τ_s^0 , μ_s , and μ_d . Peyrat *et al.* (2001) found that Landers ground motion can be equally well fit by either an asperity model, with heterogeneous initial stress, or a barrier model, with heterogeneous friction. So for the purposes of dynamic rupture simulation, there is leeway in how the dynamics can be configured. TeraShake2 used an asperity model with the dominant heterogeneity in the initial shear traction. Coefficients of friction were constant at $\mu_s = 1$ and $\mu_d = 0$. The slip-weakening displacement was constant at $d_0 = 1$ m, aside from a near-surface modification discussed next. In selecting parameters, Peyrat *et al.* (2001) noted a delicate balance between cases where rupture did not proceed at all, and cases where the rupture proceeded at supershear velocity. In order to create a model with sustained subshear rupture velocity, they found it necessary to introduce small along-strike variation of the normal stress (and therefore the friction), in the form of an along-strike increase of normal stress in the direction of rupture.

For this article, we use a modified version of one of the northwest propagating TeraShake2 scenarios with the specific version number TeraShake2.2. Our model uses coefficients of friction $\mu_s = 1.1$ and $\mu_d = 0.5$, initial normal traction $\tau_n^0 = -20$ MPa, and slip-weakening displacement $d_0 = 0.5$. Unlike TeraShake2.2, these parameters specify a

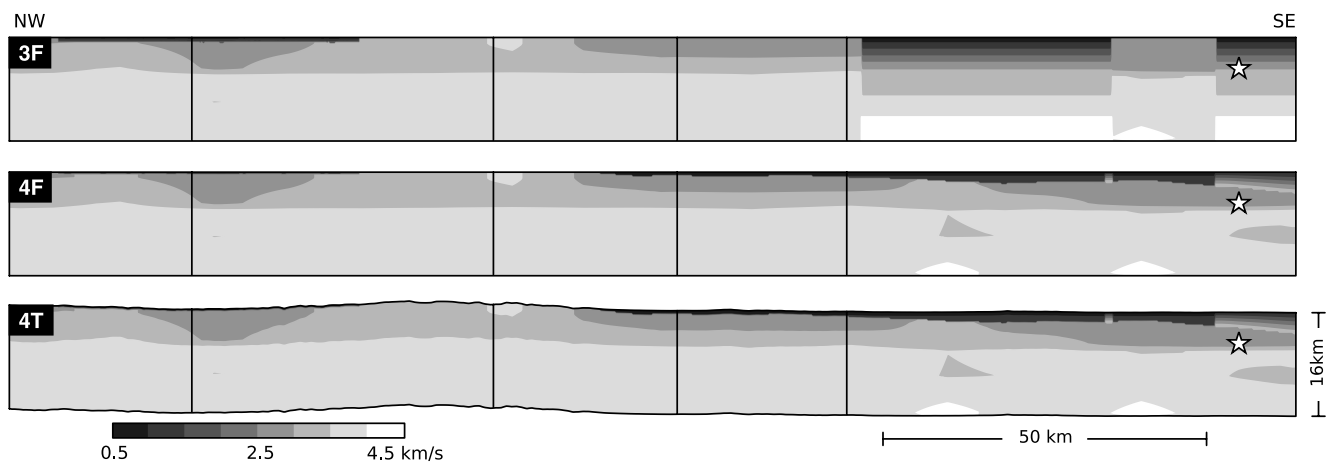


Figure 6. Comparison of S -wave velocity on the fault surface for models 3F, 4F, and 4T. Vertical lines mark changes in strike between planar segments. The stars mark the nucleation points at 5 km depth. SCEC-CVM version 3.0 is used for model 3F; version 4.0 is used for models 4F and 4T. Ground-surface topography is incorporated into model 4T and flattened to a planar surface for models 3F and 4F.

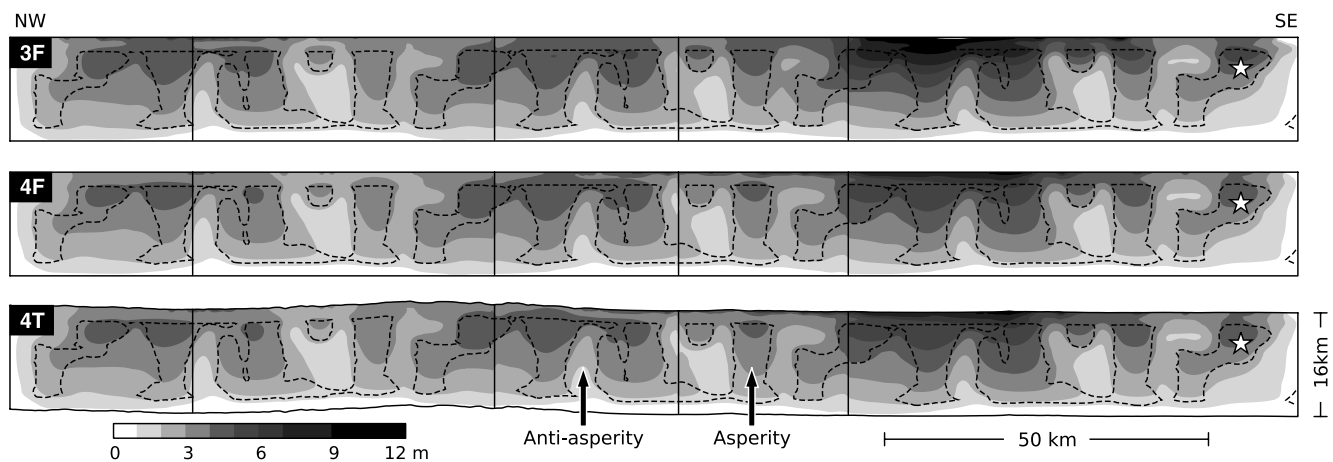


Figure 7. Comparison of final slip for models 3F, 4F, and 4T. High slip is smoothly correlated to low density basin material at the surface, and to high initial traction at depth. Areas of high initial traction (asperities) are demarcated by dashed contours at 18 MPa.

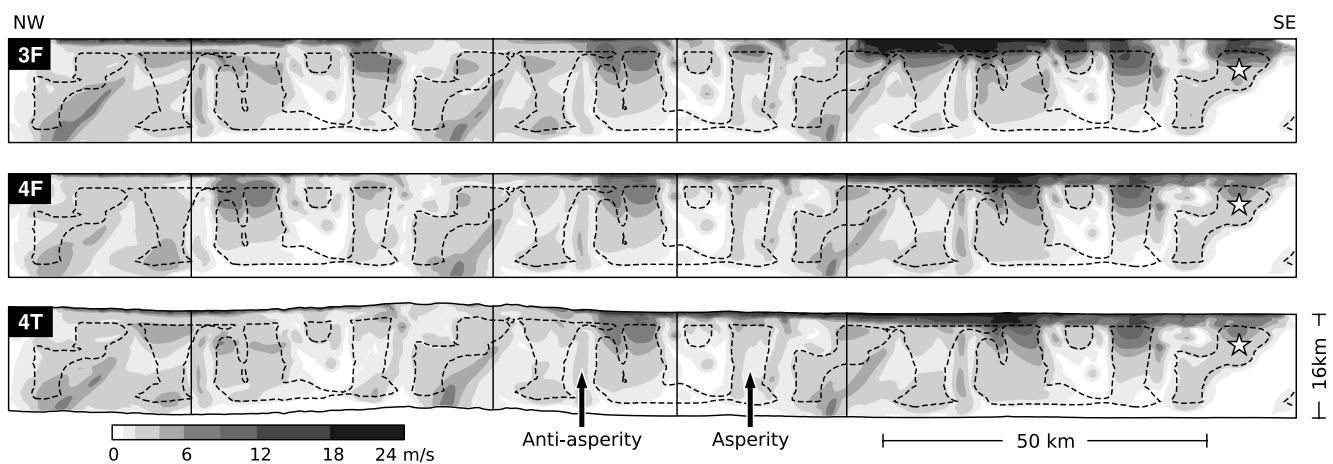


Figure 8. Comparison of peak slip rate for models 3F, 4F, and 4T. Highest slip rates at the surface occur in low density basin material. Due to rupture front focusing, highest slip rates at depth occur in narrow bands, located in areas of low initial shear traction (antiasperities).

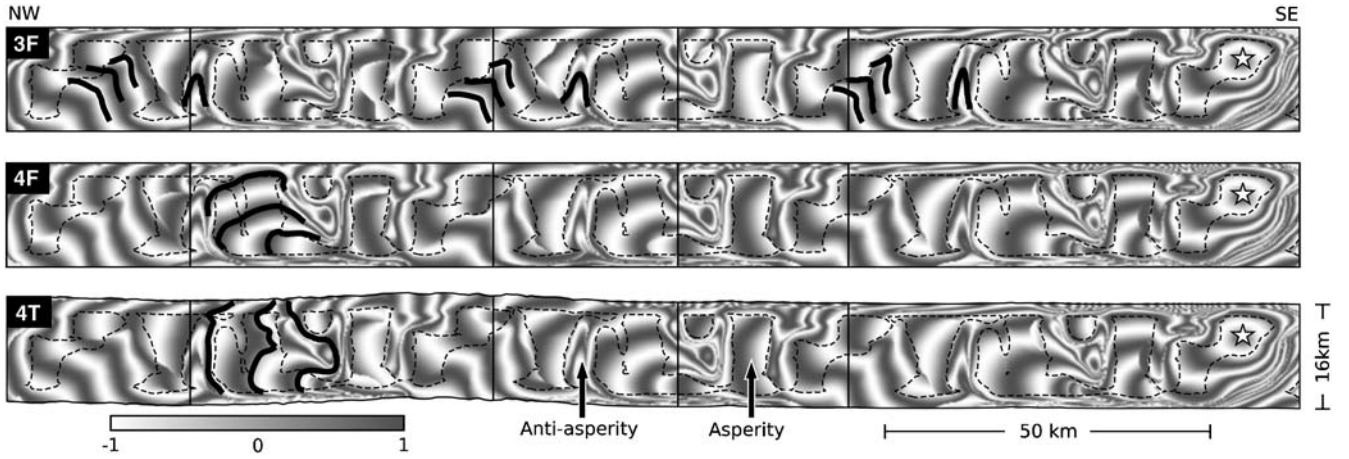


Figure 9. Isochrons of initial rupture time with 2-sec interval (displayed as $\cos(\pi t_{\text{rup}})$, where t_{rup} is the time when slip velocity first exceeds 1 cm/sec). Heavy contours in 3F highlight V-shaped focusing of rupture that produces high slip-rate bands seen in Figure 8. Heavy contours in 4T highlight rupture focusing around an antiasperity that leads to supershear rupture velocity. Similar focusing does not occur at the same location in 4F, where instead rupture takes a single path around the antiasperity, and propagates upward at subshear velocity.

nonzero dynamic friction level. This prevents reverse and oscillatory slip, and in that sense may be a better approximation of real fault behavior, though both models neglect the strong velocity dependence that is indicated by experimental evidence (e.g., [Tsutsumi and Shimamoto, 1997](#); [Beeler et al., 2007](#)) and thermal constraints on friction ([Rice, 2006](#)). The initial normal traction used here lacks depth dependence and may be unrealistically low. However, the key physical quantity responsible for radiating waves and that is resolvable by inversions, such as the Landers model, is the change in traction (or stress drop). We may be less mindful of absolute stress values and still build well-founded dynamic rupture models, provided the stress drop is realistically modeled.

For the initial shear traction model (Fig. 4), we take the TeraShake2.2 distribution, τ'_s , and apply a scale factor, an offset, and a 10% linear taper,

$$\tau_s = (0.6455\tau'_s + 10)(1.05 - 0.0005r), \quad (3)$$

where r is the horizontal distance (in km) along the fault from the southeast end. Configured as such, our models produce sustained subshear rupture, similar to TeraShake2.2, but with a reduced magnitude of $M_w = 7.6$. For comparison, various empirically derived magnitude-area scaling relations predict magnitudes of 7.56 ([Wells and Coppersmith, 1994](#)), 7.71 (Ellsworth B, equation 4.5b, [Working Group on California Earthquake Probabilities, 2003](#)), 7.55 ([Somerville, 2006](#)), and 7.75 ([Hanks and Bakun, 2002, 2008](#)) for a rupture of this size.

A problem with transplanting the Landers inversion results onto the SAF for rupture dynamic simulations is the discrepancy in velocity models at the near surface. The 1D velocity model used by [Peyrat et al. \(2001\)](#) for the inversion has a minimum S-wave velocity of 1.98 km/sec at the surface, while the minimum velocity for the rupture models is 500 m/sec. To avoid unrealistically large slip and rupture velocities near the surface, [Olsen et al. \(2008\)](#) made a number of adjustments to the dynamics parameters.

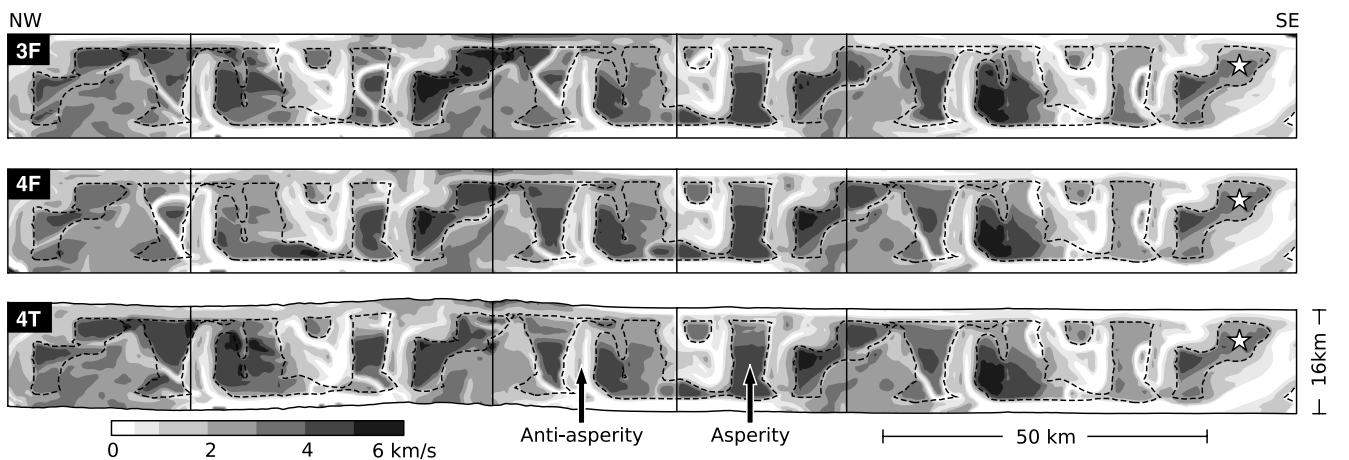


Figure 10. Comparison of spatially smoothed initial rupture velocity for models 3F, 4F, and 4T. Largest values are generally confined to asperities, with high variability among the models at the northwest end.

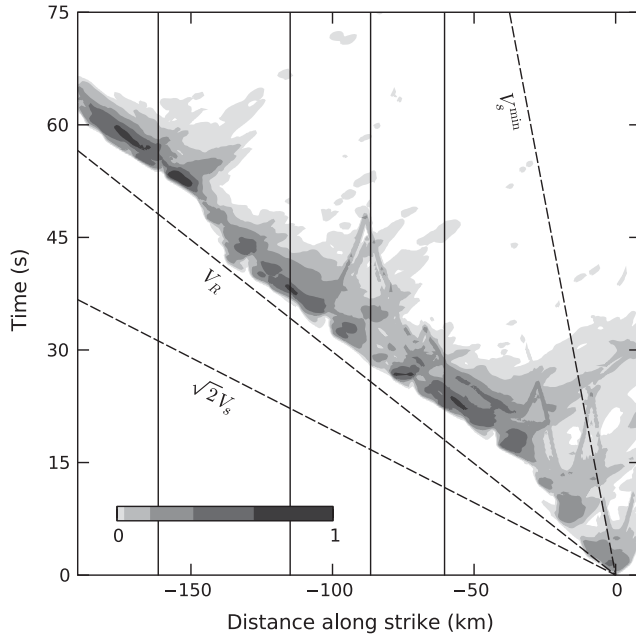


Figure 11. Space-time plot of depth averaged slip rate for model 4T, with the peak value normalized to one. In addition to the main northwest rupture pulse, secondary back-propagating ruptures and slow surface ruptures are visible as well. The overall rupture velocity is less than the mean Rayleigh velocity (V_R); local rupture velocity is bounded by the minimum S -wave velocity (V_S^{\min}) and $\sqrt{2}V_S$.

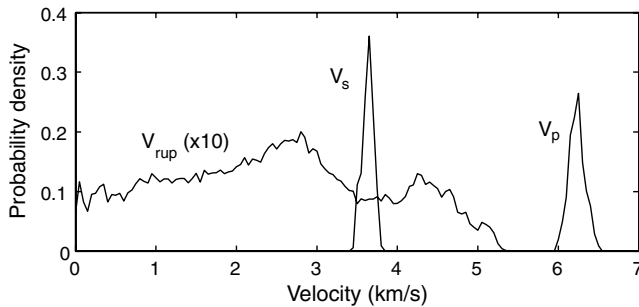


Figure 12. Distribution of rupture velocity, S -wave velocity, and P -wave velocity on the fault surface for model 4T. The sample is limited to areas where V_S and V_P are close to their median values, thus excluding the near-surface. Rupture velocity is spatially smoothed, and for display, probabilities are scaled by a factor of 10 relative to those for V_S and V_P .

The initial shear traction was tapered to 0 between 2 km and 1 km depth, and set to 0 over the 0–1 km depth range. Additionally, in the San Bernardino Valley only, initial normal traction was reduced, and dynamic slip-weakening friction was replaced with constant friction by setting d_0 to a very large number. This results in the fault being highly dissipative near the surface. In this article, we have used the same reduction of near-surface shear traction, although after the rescaling, it is no longer 0 at the surface, but about 10 MPa. We have not retained the normal traction and slip-weakening modifications. We instead opt for a simplified model with constant values over the fault. This may result in unrealistically large slip near the surface at some locations. However, it involves a relatively small percentage of the fault surface; the effect on far-field ground motions is presumably minor.

The hypocenter is located at 5 km depth, 9 km from the southeast end of the fault. Rupture is nucleated by lowering the coefficient of friction to its dynamic level (μ_d) over an expanding circular patch. The radius of the patch expands at 2300 m/sec (roughly the Rayleigh wave speed) until spontaneous rupture is able to proceed unassisted, which occurs within about 3 km of the hypocenter. Table 2 provides a summary of wave propagation and source model parameters.

Grid Generation

The average resolution for the curved hexahedral mesh is 200 m, requiring 1.8×10^9 grid points to mesh the entire volume. The coordinate system is the Universal Transverse Mercator (UTM) zone 11 projection, with the origin translated to 120° W, $34^\circ 30'$ N, and the x and y axes rotated 40° clockwise from UTM eastward and northward. The mesh has a logically rectangular structure in which nodes and cells are referenced by their logical indices j , k , and l . Grid lines of varying l (i.e., constant j , k lines) are exactly vertical so that lateral element faces are planar and vertical. We create two versions of the mesh that differ only in their z coordinate: one with a flat ground surface and one conformed to a digital elevation model. The two meshes have the same horizontal coordinates x and y , so that they appear identical in map view (Fig. 5). Terrestrial elevations are resampled from the Global Land One-km Base Elevation (GLOBE) data set; sea floor elevations are resampled from the ETOPO2 (U.S. Department of Commerce, 2006) data set. Both GLOBE and ETOPO2 are provided by the U.S. Department of

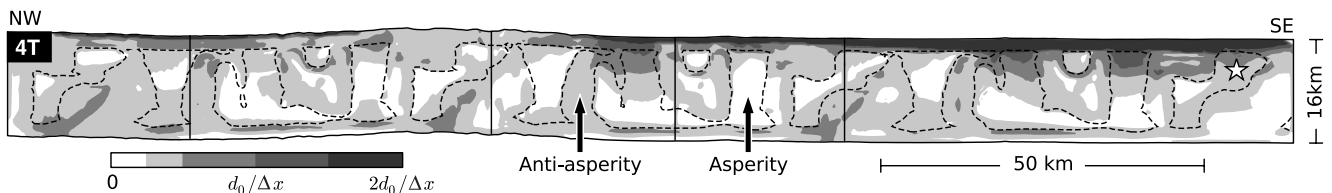


Figure 13. Peak slip gradient for model 4T. Lower gradients in the asperities ensure adequate cohesive zone resolution. Where gradients approach or exceed $d_0/\Delta x$, the cohesive zone is likely to be poorly resolved.

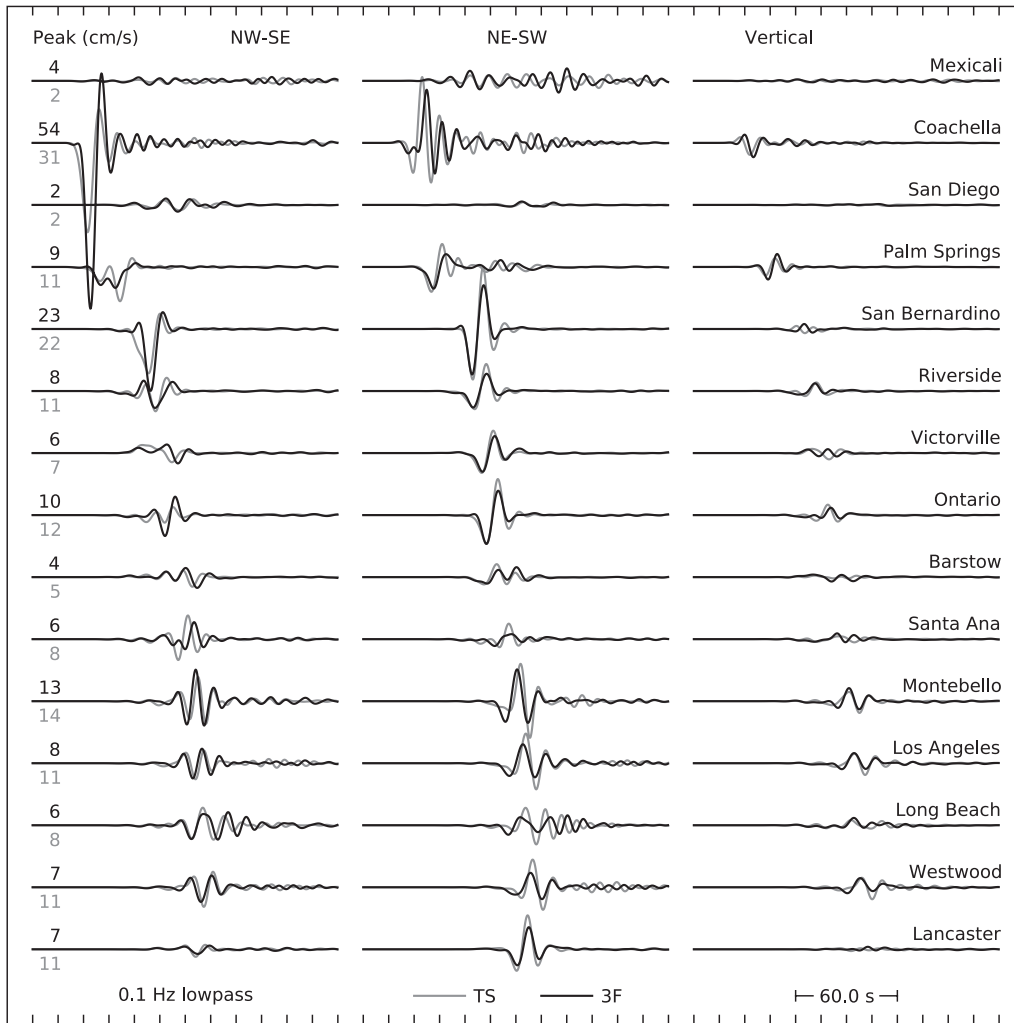


Figure 14. Zero to 0.1 Hz ground velocity for TeraShake2.2 (TS) and model 3F. The TS curves are downscaled to match the moment release of model 3F. Receiver locations are shown in Figures 1 and 2.

Commerce, National Geophysical Data Center. The minimum, maximum, and mean elevation of the topography model are -1988 , 3404 , and 379 meters, respectively. To simplify application of PML absorbing boundaries, the bottom and side boundaries are made planar and orthogonal to the Cartesian directions, and the intersecting grid lines are orthogonal to the boundaries. Special emphasis is given to ensuring the mesh is well behaved in the vicinity of the fault surface. A double layer of elements encasing the 200×16 km slipping portion of the fault is given the following properties: element faces intersecting the fault are orthogonal to the fault surface (at fault kinks the element faces bisect the kink angle); l grid line segments are vertical and exactly 200 m; the horizontal projections of j and k line segments are exactly 200 m; and each fault surface element is a parallelogram (square in the absence of topography) of area exactly equal to $40,000 \text{ m}^2$. All remaining elements throughout the volume are linearly interpolated between the fault, PML, and ground-surface elements.

Rupture Solutions

Three separate simulations were performed and given the names 3F, 4F, and 4T (Table 3). The numeric part of the name indicates the version of the SCEC-CVM used, and the letter indicates whether surface topography was included (T) or not (F). For the flattened (F) models, the mesh points and their associated materials properties are shifted downward by a distance equal to the local elevation. This procedure preserves the presence of shallow low-velocity layers at the cost of distortion to the lithologic structure. Figure 6 shows the geometry of the fault plane and the S -wave velocity for the three models. Models 3F and 4T were computed on the DataStar machine at the San Diego Supercomputer Center (SDSC) using 1920 processors. The runs took 13 hrs each, with a computation rate of 370 Gflops/sec. Model 4F was computed on the SDSC IA-64 Linux cluster, using 480 processors, and ran for 18 hrs. It was prematurely halted due to technical problems, completing 150 sec of simulation time, out of the prescribed 180 sec.

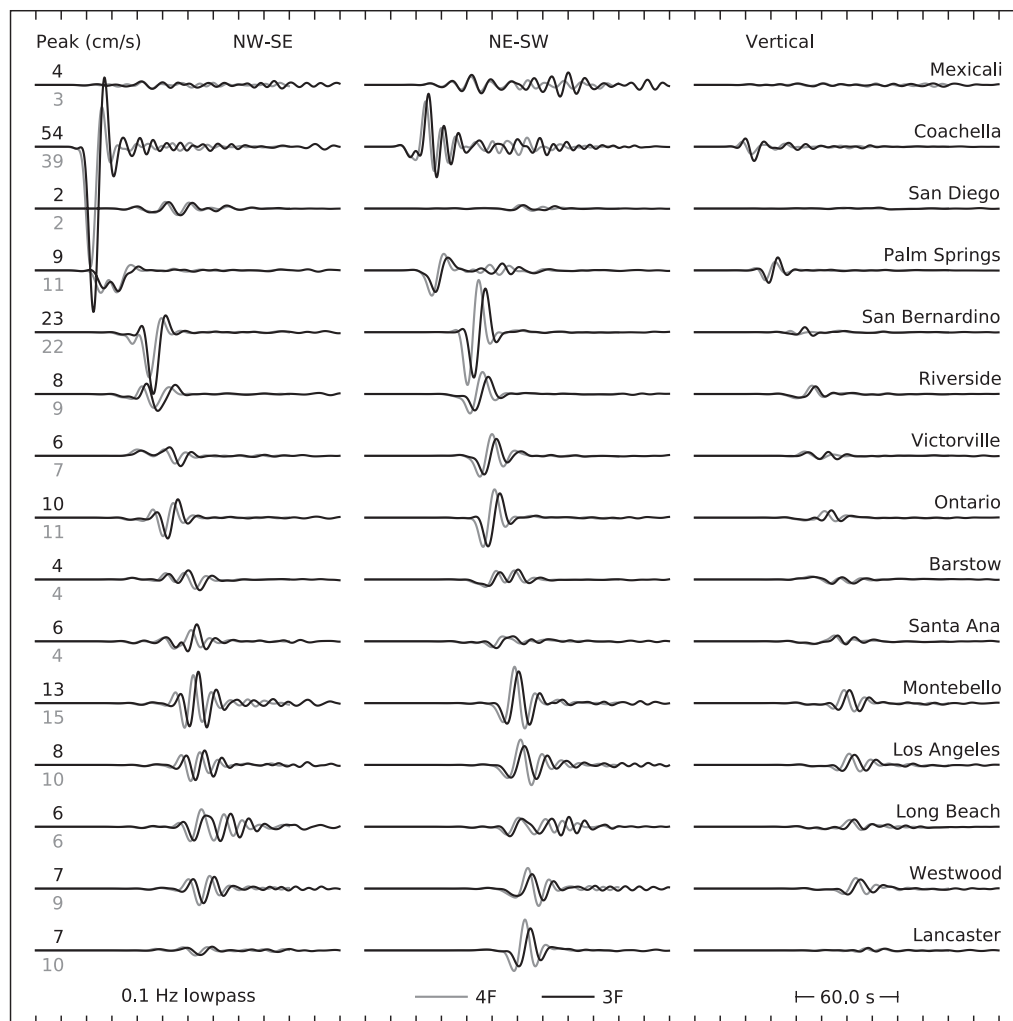


Figure 15. Zero to 0.1 Hz ground velocity for models 4F and 3F.

Due to the identical initial tractions among the models, the rupture solutions are similar at long wavelengths. This is evident in the strong likeness of the final slip distributions (Fig. 7). Shorter wavelength differences are more apparent in the peak slip rates (Fig. 8), initial rupture times (Fig. 9), and initial rupture velocities (Fig. 10, computed as the spatially smoothed magnitude of the rupture time gradient). Many of the differences can be understood through the following examination of the rupture process.

Figure 11, a space-time image of slip rate, shows that the rupture is pulselike, in the sense that slip duration at a point is short compared with overall rupture duration. Pulselike behavior can result from a friction law in which the fault restrengthens behind the rupture front (e.g., due to strong velocity dependence, as in [Beeler and Tullis, 1996](#); [Zheng and Rice, 1998](#); [Nielsen and Carlson, 2000](#)), or when slip duration is controlled by secondary scale lengths such as the seismogenic depth and/or asperity dimensions (e.g., [Day, 1982](#); [Beroza and Mikumo, 1996](#); [Day et al., 1998](#)). Only the latter mechanism operates in these simulations.

The pulselike rupture takes a circuitous path across the fault surface, following patches of high initial traction (asperities). Patches of low initial shear traction (antiasperities) generally lag behind, rupturing after the main front has passed. At some locations, delay of rupture by antiasperities leads to concavities and focusing of the rupture front into the antiasperities. V-shaped focusing, visible in the contours of initial rupture time (Fig. 9), leads to the interesting result that the highest peak slip velocities at depth (Fig. 8) are not located in highly stressed asperities, but in antiasperities.

In some cases, rupture completely encircles an antiasperity and converges to a point at its center, as described by [Das and Kostrov \(1983\)](#). [Dunham et al. \(2003\)](#) recognized this as a mechanism for generating supershear rupture velocity. We see a prominent example of this at the northwest end of the fault, which is present in models 3F and 4T, but absent in model 4F. Rupture time contours in Figure 9 highlight the location of this effect in 4T and its absence in 4F. The result is a large disparity in the rupture velocities (Fig. 10) within a number of the asperities located in the northwest half of the fault. The

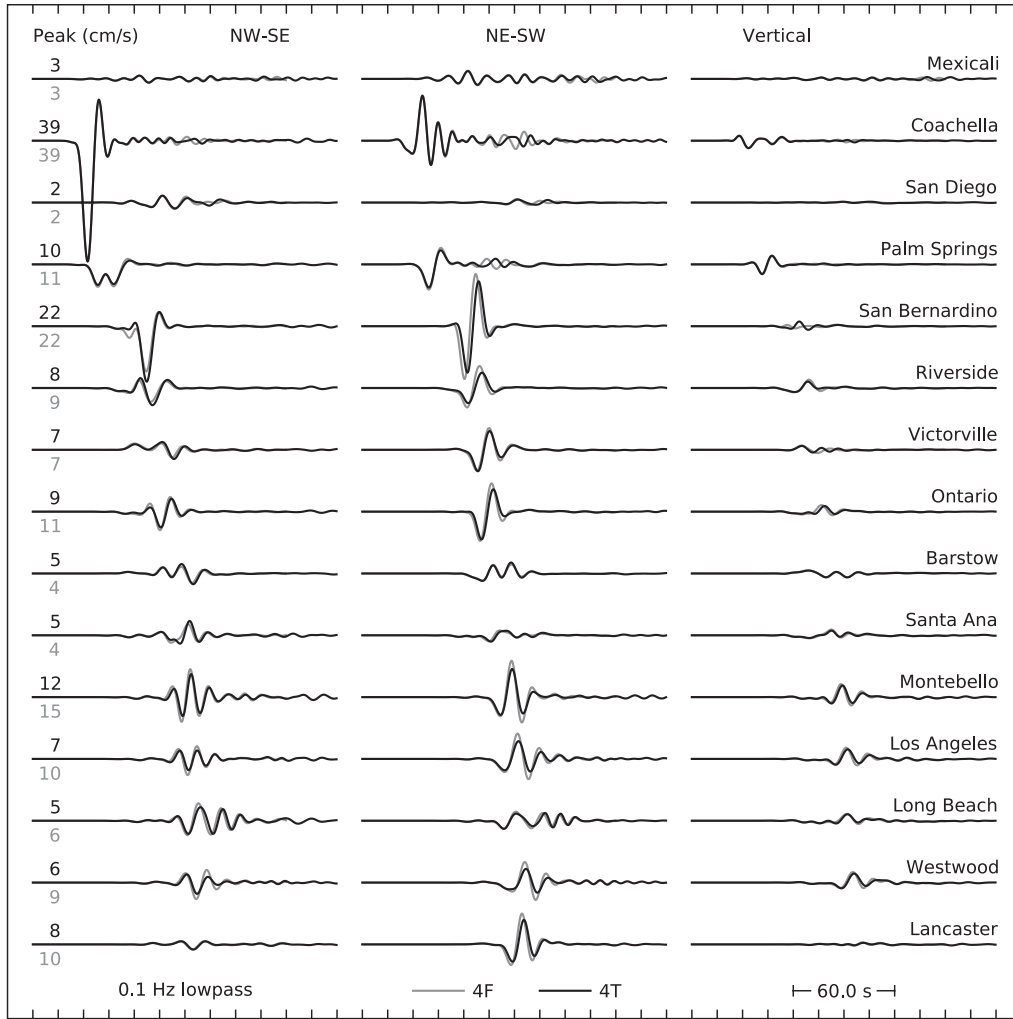


Figure 16. Zero to 0.1 Hz ground velocity for models 4F and 4T.

observation that these differences are not correlated to velocity model differences indicates that the prior rupture history has a much stronger influence on rupture velocity than the local material properties.

From the space-time slip-rate image (Fig. 11) it is clear that the overall rupture velocity is less than the mean Rayleigh velocity, V_R . A histogram of initial rupture time velocity (Fig. 12) shows a maximum value at about $0.85V_R$, a secondary maximum at about $1.2V_S$, and a minimum around V_S . This reflects that the rupture is predominantly mode II. Steady mode II ruptures are capable of propagation at velocities above V_S , but not in the interval between V_R and V_S . The distribution of rupture velocities sharply declines above $\sqrt{2}V_S$, the velocity at which S -wave radiation vanishes for mode II rupture (Eshelby, 1949).

Cohesive Zone Resolution

To ensure numerical convergence of slip-weakening rupture models, it is important to adequately resolve the cohesive zone, that is, the portion of the fault behind the rupture tip that

is actively weakening and has not yet reached the dynamic friction level. For a static, initially uniformly stressed, semi-infinite, mode II crack, Palmer and Rice (1973) and Rice (1980) estimated the cohesive zone width to be

$$\Lambda_{\text{II}}^0 = \frac{9\pi}{32} \frac{d_0\mu}{(1-\nu)(\mu_d - \mu_s)\tau_n^0}, \quad (4)$$

where μ is the shear modulus and ν is Poisson's ratio. For a mode III crack, they estimated the width to be

$$\Lambda_{\text{III}}^0 = \frac{9\pi}{32} \frac{d_0\mu}{(\mu_d - \mu_s)\tau_n^0}. \quad (5)$$

For the SCEC-CVM 4.0 models, the Λ_{II}^0 estimate ranges from 38 m at some surface locations to 2490 m at depth, with a mean of 1600 m. Λ_{III}^0 ranges from 20 to 1915 m, with a mean of 1200 m. With a spatial resolution of 200 m, the cohesive zone is likely to be poorly resolved within the low-velocity basins. This has the effect of artificially increasing d_0 , and increasing the fracture energy dissipated at the fault. Fortunately, higher d_0 may be physically appropriate for

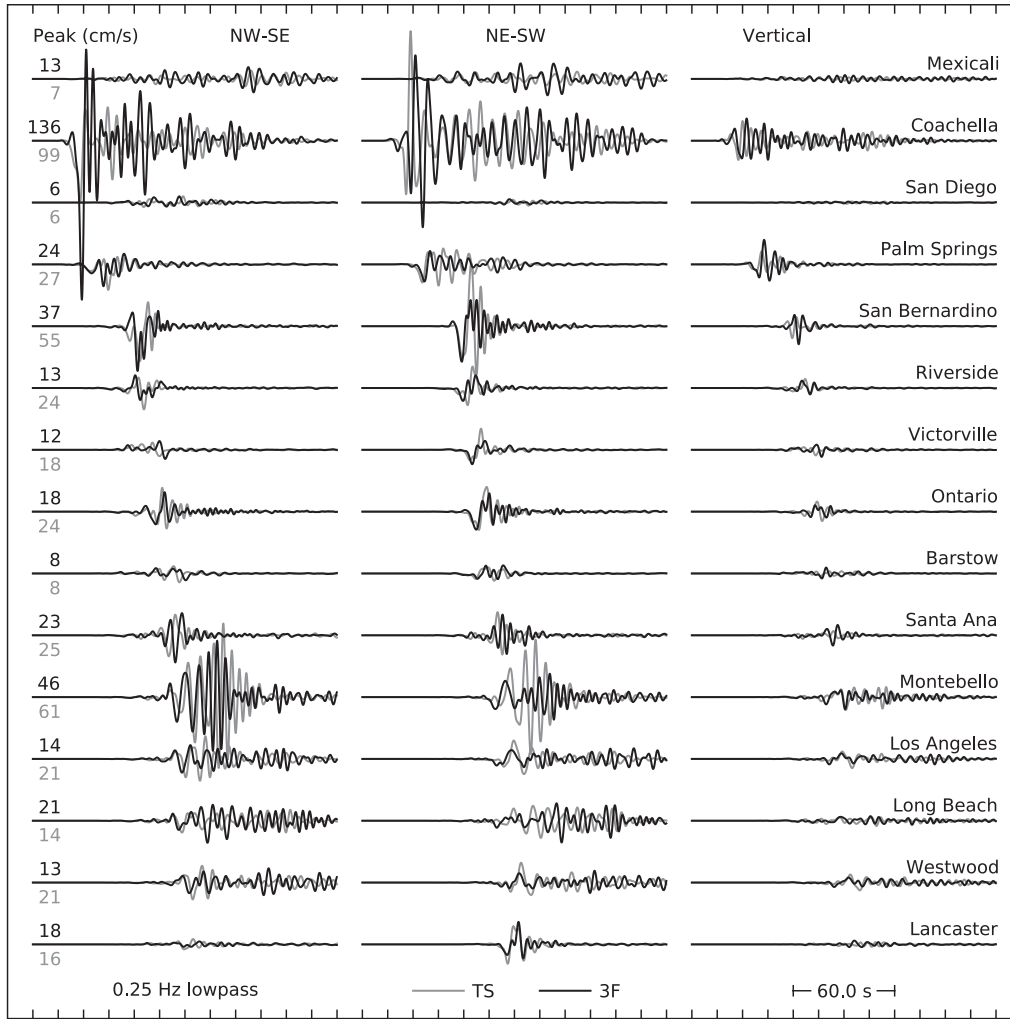


Figure 17. Zero to 0.25 Hz ground velocity for TeraShake2.2 (TS) and model 3F. The TS curves are downscaled to match the moment release of model 3F.

the near surface. As discussed previously, TeraShake2.2 specified an essentially infinite slip-weakening displacement for the San Bernardino Valley.

Equations (4) and (5) apply to a static crack and provide an upper bound for a crack tip propagating with nonzero rupture velocity. For a propagating rupture, Andrews (1976, 2004), estimates the cohesive zone width to be approximately

$$\Lambda = c \left(\frac{d_0 \mu}{\Delta \tau} \right)^2 \frac{1}{L}, \quad (6)$$

where L is the propagation distance, and c is a constant of order one for which Day *et al.* (2005) provide the rough estimate 9/16. Their analysis relies on a number of simplifying assumptions, such as a semi-infinite, 2D crack geometry. We wish to test whether the Λ estimate is useful for the complicated, heterogeneous models of this study. If asperities are treated as subfaults of approximate width 8 km and stress drop of 9 MPa, (6) gives a Λ estimate of about 290 m. That would imply that the cohesive zone is resolved by only two or three mesh points. However, this estimate based on local

asperity dimension and stress drop appears to be conservative. A lower bound Λ_{\min} can be measured directly from the rupture solutions by taking the ratio of d_0 to the peak slip gradient (plotted for model 4T in Fig. 13). For large portions of the asperities, Λ_{\min} is 800 meters or more. The mean Λ_{\min} over the fault surface is 475 meters, and the median 625 meters. The actual cohesive zone width is likely to be greater than the lower bound Λ_{\min} . However, Λ_{\min} becomes as low as 100 meters at some locations in the low-velocity sediments and cohesive zone resolution becomes poor. These cohesive zone width results can be verified visually by contouring the slip path length at the initiation of rupture and at the slip-weakening displacement, as shown in the rupture dynamics animation ⑤ available in the electronic edition of BSSA.

Ground Motion

We now consider velocity time histories for selected sites at the free surface. From here onward, where comparisons

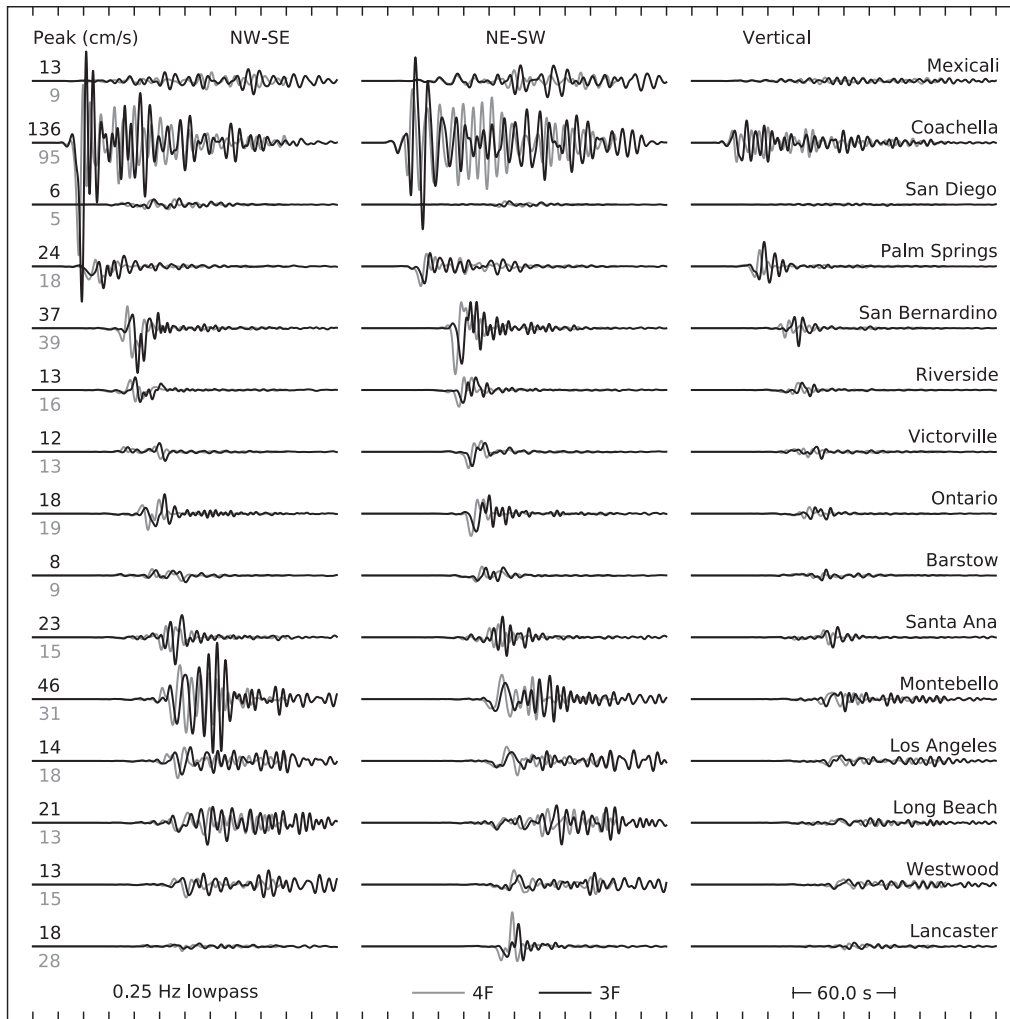


Figure 18. Zero to 0.25 Hz ground velocity for models 4F and 3F.

are made to TeraShake2.2 results, the latter are scaled by a factor of 0.674, the ratio of moment release between model 3F and TeraShake2.2. This is equivalent to scaling the TeraShake2.2 shear and normal prestress values and d_0 parameter by the same factor of 0.674. We use the abbreviation TS as shorthand for the scaled TeraShake2.2 model. At low frequency (below 0.1 Hz), the strongest velocities are generally confined to a pulse containing between one and three cycles of oscillation, and lasting 30 to 60 secs. Model 3F agrees well with TS (Fig. 14). Differences due to the velocity model are minor between models 3F and 4F (Fig. 15); the effects of topography in model 4T compared with model 4F are smaller still (Fig. 16).

At higher frequency ($0.1 < f \leq 0.25$ Hz), basin reverberations last much longer than 60 sec at some sites, and there are greater differences in ground motion among the models (Figs. 17, 18, 19). Variability in the source ruptures hinders our ability to distinguish between source and path effects as the cause of the differences. The ambiguity can be illustrated by the Lancaster site located 75 km from the end

of the rupture in the forward directivity direction. Peak ground velocity (PGV) at Lancaster is 50% greater in model 4F than in model 4T. A possible source-based explanation is that the deamplification in model 4T is caused by decrease forward directivity due to the prevalence of supershear rupture velocities at the northwest end of the fault. A path-based explanation may be that surface waves are disrupted by the topography of the San Bernardino Mountains, an effect described by (Ma *et al.* (2007).

In the case of the wave-guide amplification (clearly visible in the surface wave animation [E](#) available in the electronic edition of *BSSA*), the Los Angeles (LA) basin site of Montebello exhibits strong dependence on the velocity model. For sites lying on the shallow basin between the SAF and the LA basin (San Bernardino, Riverside, and Ontario), ground velocity time histories are similar for models 3F and 4F, suggesting that wave energy entering the LA basin is comparable for the two models. Upon reaching Montebello, however, ground velocities have 50% greater peak amplitude in 3F, due to strong energy arriving later in the record. The LA

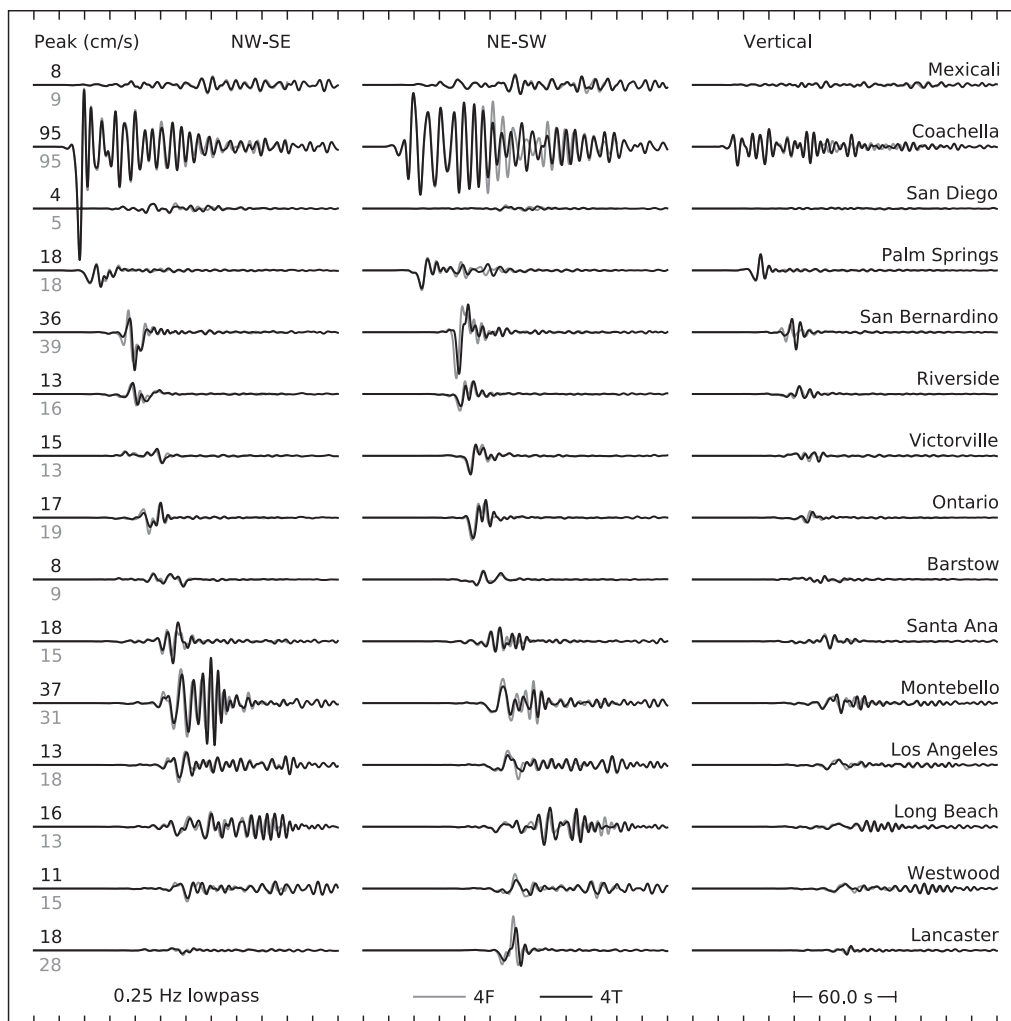


Figure 19. Zero to 0.25 Hz ground velocity for models 4F and 4T.

basin sites of Santa Ana and Long Beach show similar amplification of model 3F relative to model 4F.

For hypothetical earthquake scenarios modeling, one of the few comparisons to empirical data available is with attenuation relations. Derived from earthquake catalog statistics, attenuation relations are ground motion prediction formulas based on parameters such as moment magnitude, fault/receiver distance, basin depth, and style of faulting. For the following comparison, we use the Next Generation Attenuation relation of [Campbell and Bozorgnia \(2008\)](#), abbreviated as CB-NGA.

Tables 4 and 5 list 21 receiver sites for the locations shown in Figure 2. The site specific CB-NGA parameters for this study are: R_{RUP} , the closest distance to the coseismic rupture surface; $Z_{2.5}$, the basin depth defined by the shallowest depth to S -wave velocity greater than 2.5 km/sec; and V_{S30} , the average S -wave velocity of the upper 30 m. The CB-NGA does not include a parameter for directivity or 3D path effects. We compute the pseudospectral velocity (PSV) spectra for each site and each simulation, taking the geo-

metric mean of the horizontal components (which is usually a good approximation to the GMROtI50 measure used in CB-NGA). PSV is tabulated at 5-sec period, by first smoothing the spectra with a running mean of width equal to 1/2 of the period in log-space, so the 5-sec period values represent the mean of the range 3.9 to 6.4 secs. We also give the CB-NGA median predicted PSV and 68 percent confidence limits (given by $Ye^{\pm\sigma}$, where Y is the median value and σ is the standard deviation of $\ln Y$). The PSV values are also presented graphically in Figure 20.

The sites are grouped into rock sites ($Z_{2.5} = 0$), shallow basin sites ($0.2 \leq Z_{2.5} \leq 1.2$ km), and deep basin sites ($2.4 \leq Z_{2.5} \leq 3.9$ km). The near-surface S -wave velocity (V_{S30}) is extracted from the SCEC-CVM (and is often less than the 500 m/sec minimum S -wave velocity used in the computations). Outside of the basins, surface layers are not well resolved by the SCEC-CVM, resulting in unrealistically high velocities at the rock sites. In those cases, for the purpose of evaluating the CB-NGA equation, we impose an upper limit of 760 m/sec for V_{S30} .

Table 4

Pseudospectral Velocity (Geometric Mean Horizontal Component) at 5-sec Period for TeraShake2.2 and Model 3F Compared with Campbell and Bozorgnia (2008) Median and 68% Confidence Limits ($\pm\sigma$)^{*}

Sites	R_{RUP} (km) [†]	$Z_{2.5}$ (km) [‡]	V_{S30} (m/sec) [§]	5-sec Pseudospectral Velocity (cm/sec)				
				TeraShake2.2	Model 3F	Campbell and Bozorgnia (2008) Median	$-\sigma$	$+\sigma$
Rock Sites								
Yuma	123	0.0	760	1.7	2.6	5.2	2.6	10.5
Ensenada	184	0.0	760	6.8	8.0	3.9	1.9	7.9
San Diego	145	0.0	760	9.9	8.3	4.7	2.3	9.4
Oceanside	103	0.0	760	7.8	11.1	5.9	2.9	11.9
Palm Springs	12	0.0	760	43.3	34.9	26.7	13.3	53.9
Victorville	33	0.0	760	21.2	15.5	13.1	6.5	26.4
Barstow	80	0.0	760	13.0	14.4	7.1	3.5	14.2
Lancaster	74	0.0	760	18.5	17.9	7.5	3.7	15.1
Bakersfield	184	0.0	760	6.9	12.7	3.9	1.9	7.9
Santa Barbara	203	0.0	760	6.2	4.1	3.7	1.8	7.4
Shallow Basin Sites								
San Bernardino	7	1.0	281	103.9	80.4	111.4	55.3	224.3
Riverside	27	0.8	395	35.2	30.8	33.5	16.6	67.4
Ontario	29	1.2	395	48.5	41.1	33.7	16.7	67.8
Deep Basin Sites								
Mexicali	80	3.9	739	15.0	29.5	12.1	6.0	24.3
Coachella	4	3.9	739	142.3	237.3	80.7	40.1	162.5
Montebello	64	3.5	409	185.8	134.5	21.2	10.5	42.7
Santa Ana	69	2.6	274	42.1	59.2	24.4	12.1	49.2
Long Beach	86	2.9	364	34.9	61.4	16.6	8.2	33.4
Los Angeles	73	2.8	384	35.4	41.5	17.8	8.8	35.8
Westwood	88	3.3	386	31.2	35.3	16.7	8.3	33.7
Oxnard	155	3.2	302	44.7	34.3	13.3	6.6	26.9

^{*}The TeraShake2.2 values are downscaled to a comparable M_w 7.6 event.

[†] R_{RUP} is the closest distance to the coseismic rupture surface.

[‡] $Z_{2.5}$ is the depth to the 2.5 km/sec shear velocity horizon (basin depth).

[§] V_{S30} is the average shear velocity for the upper 30 m.

The rock sites make a useful set of receivers from which to look for rupture directivity effects, where records are less obscured by basin effects. The CB-NGA does not consider directivity in its parameterization, so differences when compared with simulated ground motion that are correlated to source/receiver azimuth may likely be attributed to directivity. The rock sites are listed roughly in southeast to northwest order from Yuma to Santa Barbara. Five-sec PSV generally falls within one standard deviation of the median CB-NGA prediction. The exceptions are Yuma to the southeast that is significantly overpredicted by CB-NGA, as well as Lancaster and Bakersfield to the northwest that are significantly underpredicted, which would appear to confirm that directivity effects are detectable in the 5-sec PSV values.

Shallow basin sites generally have the lowest simulated PSV relative to the predicted CB-NGA values. We speculate that the simulation bandwidth is not able to entirely capture the dominant shallow basin reverberation frequencies, so PSV values are underestimated. Deep basin sites, where dominant wavelengths are longer and frequencies lower, are more completely captured by the simulation bandwidth. Deep basin PSVs are consistently above the CB-NGA expected values, and more so for the SCEC-CVM version 3.0

models (TS and 3F). Simulated PSVs are exceptionally high at Montebello, though not as high in our models as in TS: 5-sec PSV for TS is a factor of 9 greater than the median CB-NGA at that site, whereas for our models 5-sec PSVs are only a factor of 5 to 6 above the median CB-NGA.

The single 5-sec PSV parameter is a useful, but limited characterization of ground motion. For a more complete picture we provide the full (unsmoothed) PSV spectra and PGV values for a limited set of stations in Figures 21 and 22. The spectra reveal that the relative difference with CB-NGA can vary by as much as a factor of 5 (at Mexicali), and that the peak PSV frequency is highly site-dependent.

Conclusion

We have simulated an M_w 7.6, northwest propagating dynamic rupture on the southern San Andreas fault with non-planar fault geometry and surface topography. Numerous cases of rupture front focusing (due to heterogeneous initial stress conditions and complex rupture propagation) lead to high peak slip velocities in relatively weakly stressed antiasperities. Peak slip displacements, on the other hand, are confined to the highly stressed asperities. This suggests a

Table 5

Pseudospectral Velocity (Geometric Mean Horizontal Component) at 5-sec Period for Models 4F and 4T Compared with Campbell and Bozorgnia (2008) Median and 68% Confidence Limits ($\pm\sigma$)

Sites	R_{RUP} (km) [*]	$Z_{2.5}$ (km) [†]	V_{S30} m/sec [‡]	5-sec Pseudospectral Velocity (cm/sec)				
				Model 4F	Model 4T	Campbell and Bozorgnia (2008) Median	$-\sigma$	$+\sigma$
Rock Sites								
Yuma	123	0.0	760	2.9	3.5	5.2	2.6	10.5
Ensenada	184	0.0	760	5.6	6.0	3.9	1.9	7.9
San Diego	145	0.0	760	7.7	7.5	4.7	2.3	9.4
Oceanside	103	0.0	760	11.7	10.7	5.9	2.9	11.9
Victorville	33	0.0	760	15.9	18.0	13.1	6.5	26.4
Barstow	80	0.0	760	11.7	10.4	7.1	3.5	14.2
Lancaster	74	0.0	760	21.8	15.6	7.5	3.7	15.1
Bakersfield	184	0.0	760	10.8	12.7	3.9	1.9	7.9
Santa Barbara	203	0.0	760	5.0	5.1	3.7	1.8	7.4
Shallow Basin Sites								
Palm Springs	12	0.2	760	28.0	26.1	28.8	14.3	57.9
San Bernardino	7	0.5	281	58.7	56.7	97.3	48.3	195.9
Riverside	27	0.4	395	30.3	25.8	29.8	14.8	60.1
Ontario	29	0.5	395	32.7	36.4	28.6	14.2	57.6
Deep Basin Sites								
Mexicali	80	2.7	760	23.0	21.9	9.5	4.7	19.2
Coachella	4	2.8	760	182.6	177.0	63.6	31.6	128.1
Montebello	64	3.4	409	101.9	98.2	20.4	10.2	41.2
Santa Ana	69	2.4	274	41.5	44.0	24.4	12.1	49.2
Long Beach	86	2.8	364	49.0	60.0	16.6	8.2	33.4
Los Angeles	73	2.7	384	26.9	29.5	17.8	8.8	35.8
Westwood	88	3.1	386	19.9	19.2	16.0	8.0	32.3
Oxnard	155	3.0	302	33.69	32.8	12.8	6.4	25.8

^{*} R_{RUP} is the closest distance to the coseismic rupture surface.

[†] $Z_{2.5}$ is the depth to the 2.5 km/sec shear velocity horizon (basin depth).

[‡] V_{S30} is the average shear velocity for the upper 30 m.

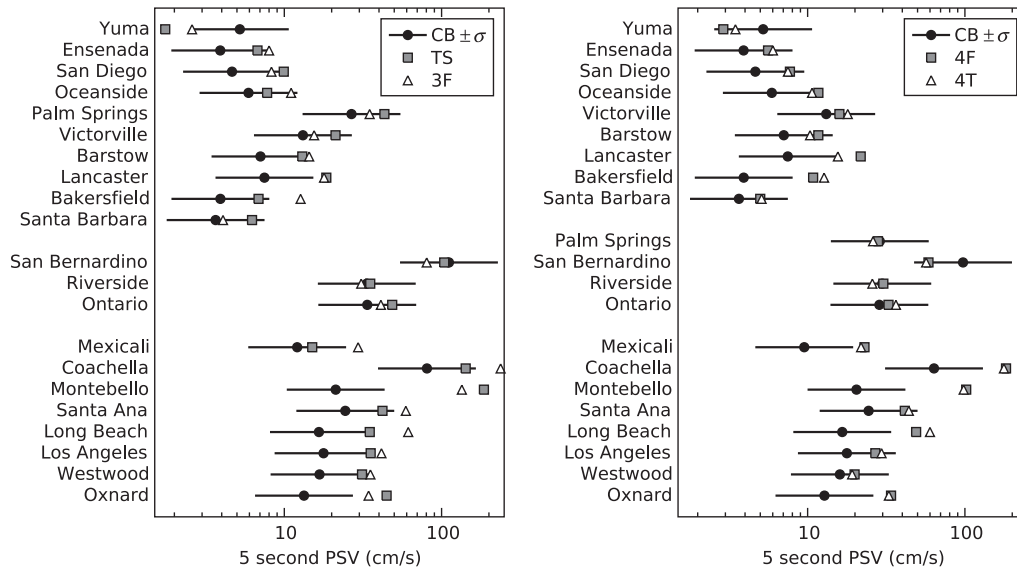


Figure 20. Plots of 5-sec period pseudospectral velocity (PSV) values from Tables 4 and 5. Campbell and Bozorgnia (2008) median and 68 percent confidence interval ($CB \pm \sigma$) are compared with scaled TeraShake2.2 and model 3F (left), and with models 4F and 4T (right).

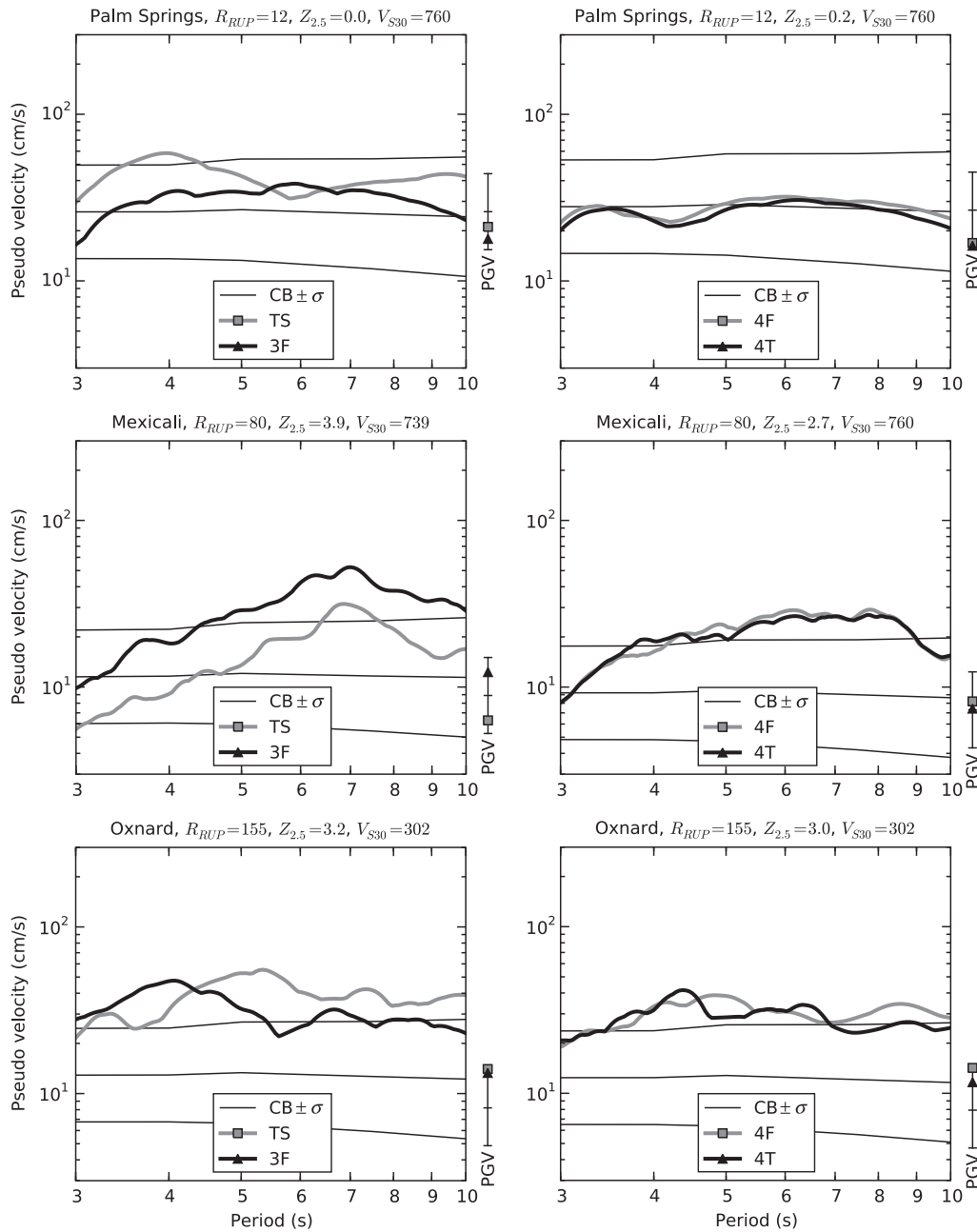


Figure 21. Pseudovelocity spectra and peak ground velocity (PGV) for Palm Springs, Mexicali, and Oxnard sites. Campbell and Bozorgnia (2008) median and 68 percent confidence limits ($CB \pm \sigma$) are compared with downscaled TeraShake2.2 (TS) and model 3F (left), and with models 4F and 4T (right).

mechanism by which high-frequency components of the slip function are at least partially disjointed from low-frequency components. A further effect of the rupture heterogeneity is that, for our simulations, the cohesive zone is generally narrower in the antiasperities than in asperities, contrary to the rough *a priori* estimates derived from steady state, semi-infinite rupture.

We compared simulations with different versions of the SCEC-CVM, and simulations with and without topography at

the free surface, and find that either change is enough to significantly alter the rupture. At low frequency, the results match the TeraShake2.2 simulation by Olsen *et al.* (2008), though our model predicts less pronounced wave-guide amplification in the LA basin. We found that the wave-guide effect is smaller still when SCEC-CVM version 4.0 is used, compared with version 3.0. Peak ground velocities for most sites fall within one standard deviation of the Campbell and Bozorgnia (2008) empirical attenuation relation. However,

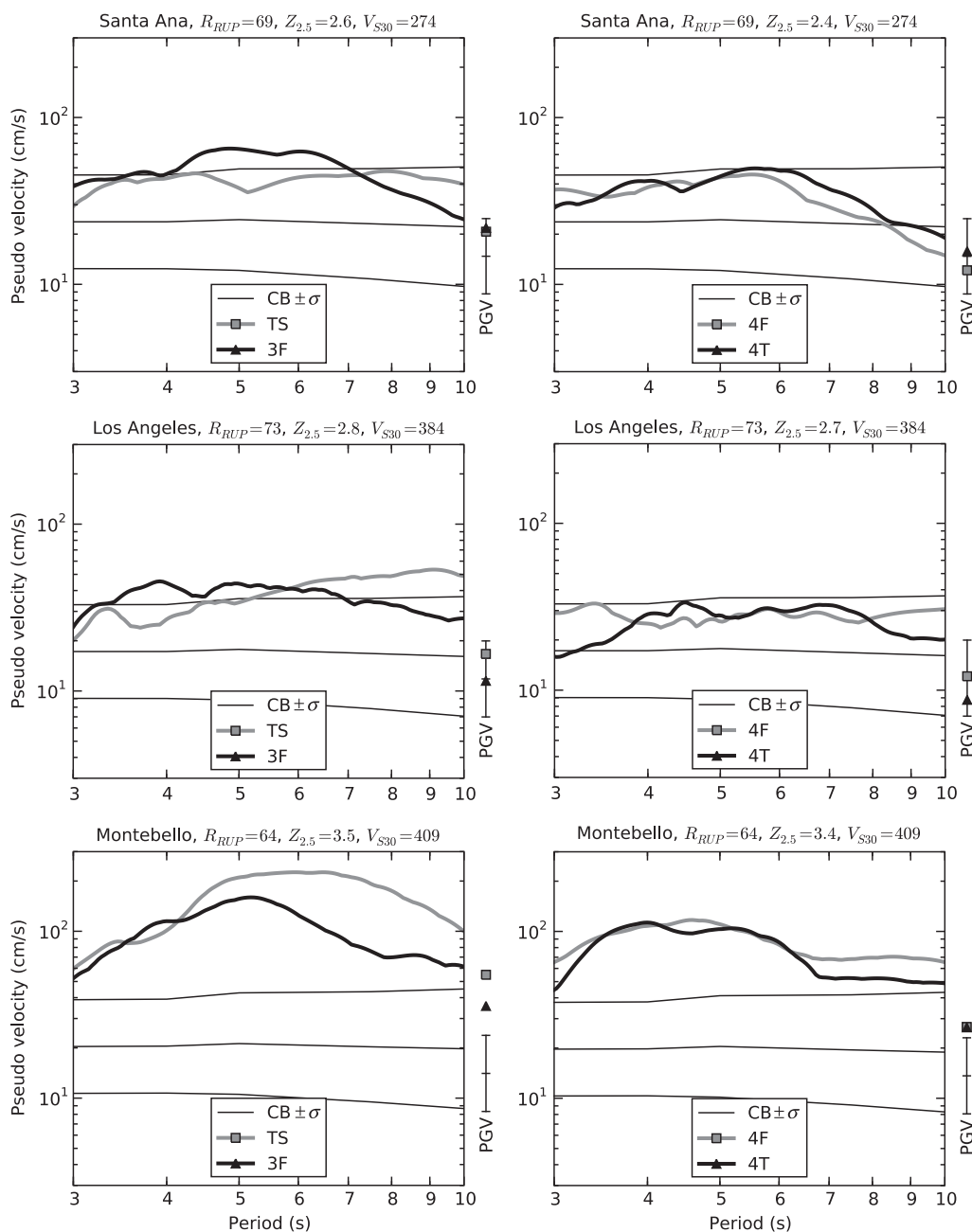


Figure 22. Pseudovelocity spectra and peak ground velocity (PGV) for Santa Ana, Los Angeles, and Montebello sites. Campbell and Bozorgnia (2008) median and 68 percent confidence limits ($CB \pm \sigma$) are compared with downscaled TeraShake2.2 (TS) and model 3F (left), and with models 4F and 4T (right).

rupture directivity and basin wave-guide effects cause more significant deviation from the attenuation relation at some sites.

Data and Resources

The Support Operator Rupture Dynamics (SOR) code used in this article, last accessed September 2007, is available at <http://earth.usc.edu/~gely/sord/>. The GLOBE and ETOPO2 topographic data sets, last accessed July 2006,

are available from the U.S. Department of Commerce, National Geophysical Data Center <http://www.ngdc.noaa.gov/mgg/topo/>.

Acknowledgments

Kim Olsen provided much assistance to the project and provided his TeraShake stress model and results for comparison. This article was supported by the National Science Foundation (NSF) under grants ATM-0325033 and EAR-0122464, by the San Diego Supercomputer Center, and by the Southern California Earthquake Center (SCEC). SCEC is funded

by NSF Cooperative Agreement EAR-0106924 and USGS Cooperative Agreement 02HQAG0008. The SCEC contribution number for this article is 1147.

References

- Andrews, D. J. (1976). Rupture propagation with finite stress in antiplane strain, *J. Geophys. Res.* **81**, no. B20, 3575–3582.
- Andrews, D. J. (2004). Rupture models with dynamically determined breakdown displacement, *Bull. Seismol. Soc. Am.* **94**, no. 3, 769–775, doi [10.1785/0120030142](https://doi.org/10.1785/0120030142).
- Beeler, N. M., and T. E. Tullis (1996). Self-healing slip pulses in dynamic rupture models due to velocity-dependent strength, *Bull. Seismol. Soc. Am.* **86**, no. 4, 1130–1148.
- Beeler, N. M., T. E. Tullis, and D. Goldsby (2008). Constitutive relationships and physical basis of fault strength due to flash-heating, *J. Geophys. Res.* **113**, no. B01401, doi [10.1029/2007JB004988](https://doi.org/10.1029/2007JB004988).
- Berenger, J.-P. (1994). A perfectly matched layer for the absorption of electromagnetic waves, *J. Comput. Phys.* **114**, no. 2, 185–200, doi [10.1006/jcph.1994.1159](https://doi.org/10.1006/jcph.1994.1159).
- Berenger, J.-P. (1996). Three-dimensional perfectly matched layer for the absorption of electromagnetic waves, *J. Comput. Phys.* **127**, no. 2, 363–379, doi [10.1006/jcph.1996.0181](https://doi.org/10.1006/jcph.1996.0181).
- Beroza, G. C., and T. Mikumo (1996). Short slip duration in dynamic rupture in the presence of heterogeneous fault properties, *J. Geophys. Res.* **101**, no. B10, 22,449–22,460, doi [10.1029/96JB02291](https://doi.org/10.1029/96JB02291).
- Campbell, K. W., and Y. Bozorgnia (2008). NGA ground motion model for the geometric mean horizontal component of PGA, PGV, PGD and 5% damped linear elastic response spectra for periods ranging from 0.01 to 10 s, *Earthquake Spectra* **24**, no. 1, 139–171, doi [10.1193/1.2857546](https://doi.org/10.1193/1.2857546).
- Das, S., and B. V. Kostrov (1983). Breaking of a single asperity: Rupture process and seismic radiation, *J. Geophys. Res.* **88**, no. B5, 4277–4288.
- Day, S. M. (1982). Three-dimensional finite difference simulation of fault dynamics: Rectangular faults with fixed rupture velocity, *Bull. Seismol. Soc. Am.* **72**, no. 3, 705–727.
- Day, S. M. (1998). Efficient simulation of constant Q using coarse-grained memory variables, *Bull. Seismol. Soc. Am.* **88**, no. 4, 1051–1062.
- Day, S. M., and C. R. Bradley (2001). Memory-efficient simulation of anelastic wave propagation, *Bull. Seismol. Soc. Am.* **91**, no. 3, 520–531, doi [10.1785/0120000103](https://doi.org/10.1785/0120000103).
- Day, S. M., L. A. Dalgner, N. Lapusta, and Y. Liu (2005). Comparison of finite difference and boundary integral solutions to three-dimensional spontaneous rupture, *J. Geophys. Res.* **110**, B12307, doi [10.1029/2005JB003813](https://doi.org/10.1029/2005JB003813).
- Day, S. M., G. Yu, and D. J. Wald (1998). Dynamic stress changes during earthquake rupture, *Bull. Seismol. Soc. Am.* **88**, no. 2, 512–522.
- Dunham, E. M., P. Favreau, and J. M. Carlson (2003). A supershear transition mechanism for cracks, *Science* **299**, no. 5612, 1557–1559, doi [10.1126/science.1080650](https://doi.org/10.1126/science.1080650).
- Ely, G. P., S. M. Day, and J.-B. H. Minster (2008). A support-operator method for viscoelastic wave modeling in 3D heterogeneous media, *Geophys. J. Int.* **172**, no. 1, 331–344, doi [10.1111/j.1365-246X.2007.03633.x](https://doi.org/10.1111/j.1365-246X.2007.03633.x).
- Ely, G. P., S. M. Day, and J.-B. H. Minster (2009). A support-operator method for 3D rupture dynamics, *Geophys. J. Int.* **177**, no. 3, 1140–1150, doi [10.1111/j.1365-246X.2009.04117.x](https://doi.org/10.1111/j.1365-246X.2009.04117.x).
- Eshelby, J. D. (1949). Uniformly moving dislocations, *Proc. Phys. Soc. A* **62**, no. 5, 307–314, doi [10.1088/0370-1298/62/5/307](https://doi.org/10.1088/0370-1298/62/5/307).
- Frankel, A. (1993). Three-dimensional simulations of ground motions in the San Bernardino Valley, California, for hypothetical earthquakes on the San Andreas fault, *Bull. Seismol. Soc. Am.* **83**, no. 4, 1020–1041.
- Frankel, A. D., M. D. Petersen, C. S. Mueller, K. M. Haller, R. L. Wheeler, E. V. Leyendecker, R. L. Wesson, S. C. Harmsen, C. H. Cramer, D. M. Perkins, and K. S. Rukstales (2002). Documentation for the 2002 update of the national seismic hazard maps, *U.S. Geol. Surv. Open File Rept. 2002-420*, Denver, Colorado.
- Graves, R. W. (1998). Three-dimensional finite-difference modeling of the San Andreas fault: Source parameterization and ground-motion levels, *Bull. Seismol. Soc. Am.* **88**, no. 4, 881–897.
- Hanks, T. C., and W. H. Bakun (2002). A bilinear source-scaling model for M -log A observations of continental earthquakes, *Bull. Seismol. Soc. Am.* **92**, no. 5, 1841–1846, doi [10.1785/0120010148](https://doi.org/10.1785/0120010148).
- Hanks, T. C., and W. H. Bakun (2008). M -log A observations for recent large earthquakes, *Bull. Seismol. Soc. Am.* **98**, no. 1, 490–494, doi [10.1785/0120070174](https://doi.org/10.1785/0120070174).
- Hughes, T. J. R. (2000). *The Finite Element Method: Linear Static and Dynamic Finite Element Analysis*, Dover Publishers, New York.
- Kohler, M. D., H. Magistrale, and R. W. Clayton (2003). Mantle heterogeneities and the SCEC reference three-dimensional seismic velocity model version 3, *Bull. Seismol. Soc. Am.* **93**, no. 2, 757–774, doi [10.1785/0120020017](https://doi.org/10.1785/0120020017).
- Ma, S., R. J. Archuleta, and M. T. Page (2007). Effects of large-scale surface topography on ground motions, as demonstrated by a study of the San Gabriel mountains, Los Angeles, California, *Bull. Seismol. Soc. Am.* **97**, no. 6, 2066–2079, doi [10.1785/0120070040](https://doi.org/10.1785/0120070040).
- Magistrale, H. (2005). Version 4 of the CVM, 2005 SCEC Annual Meeting, Palm Springs, California.
- Magistrale, H., S. M. Day, R. W. Clayton, and R. W. Graves (2000). The SCEC southern California reference three-dimensional seismic velocity model version 2, *Bull. Seismol. Soc. Am.* **90**, no. 6B, S65–76, doi [10.1785/0120000510](https://doi.org/10.1785/0120000510).
- Marcinkovich, C., and K. Olsen (2003). On the implementation of perfectly matched layers in a three-dimensional fourth-order velocity-stress finite difference scheme, *J. Geophys. Res.* **108**, no. B5, doi [10.1029/2002JB002235](https://doi.org/10.1029/2002JB002235).
- Nielsen, S. B., and J. M. Carlson (2000). Rupture pulse characterization: Self-healing, self-similar, expanding solutions in a continuum model of fault dynamics, *Bull. Seismol. Soc. Am.* **90**, no. 6, 1480–1497, doi [10.1785/0120000021](https://doi.org/10.1785/0120000021).
- Oglesby, D. D., D. S. Dreger, R. A. Harris, N. Ratchkovski, and R. Hansen (2004). Inverse kinematic and forward dynamic models of the 2002 Denali fault earthquake, Alaska, *Bull. Seismol. Soc. Am.* **94**, no. 6B, S214–233, doi [10.1785/0120040620](https://doi.org/10.1785/0120040620).
- Olsen, K. B., S. M. Day, J.-B. Minster, Y. Cui, A. Chourasia, M. Faerman, R. Moore, P. Maechling, and T. Jordan (2006). Strong shaking in Los Angeles expected from southern San Andreas earthquake, *Geophys. Res. Lett.* **33**, L07305, doi [10.1029/2005GL025472](https://doi.org/10.1029/2005GL025472).
- Olsen, K. B., S. M. Day, J.-B. Minster, Y. Cui, A. Chourasia, D. Okaya, P. Maechling, and T. Jordan (2008). TeraShake2: Spontaneous rupture simulations of M_w 7:7 earthquakes on the southern San Andreas fault, *Bull. Seismol. Soc. Am.* **98**, no. 3, 1162–1185, doi [10.1785/0120070148](https://doi.org/10.1785/0120070148).
- Palmer, A. C., and J. R. Rice (1973). The growth of slip surfaces in the progressive failure of over-consolidated clay, *Proc. R. Soc. A* **332**, no. 1591, 527–548, doi [10.1098/rspa.1973.0040](https://doi.org/10.1098/rspa.1973.0040).
- Peyrat, S., K. B. Olsen, and R. Madariaga (2001). Dynamic modeling of the 1992 Landers earthquake, *J. Geophys. Res.* **106**, no. B11, 26,467–26,482, doi [10.1029/2001JB000205](https://doi.org/10.1029/2001JB000205).
- Rice, J. R. (1980). The mechanics of earthquake rupture, in *Physics of the Earth's Interior, Proceedings of the Enrico Fermi International School of Physics*, vol. Course 78, A. M. Dziewonski and E. Boschi (Editors), 555–649, North-Holland.
- Rice, J. R. (2006). Heating and weakening of faults during earthquake slip, *J. Geophys. Res.* **111**, B05311, doi [10.1029/2005JB004006](https://doi.org/10.1029/2005JB004006).
- Seeber, L., and J. G. Armbruster (1995). The San Andreas fault system through the Transverse Ranges as illuminated by earthquakes, *J. Geophys. Res.* **100**, no. B5, 8285–8310, doi [10.1029/94JB02939](https://doi.org/10.1029/94JB02939).
- Somerville, P. G. (2006). Review of magnitude-area scaling of crustal earthquakes, *Report to the Working Group on California Earthquake Probabilities*, URS Corp., Pasadena, California.

- Tsutsumi, A., and T. Shimamoto (1997). High-velocity frictional properties of gabbro, *Geophys. Res. Lett.* **24**, no. 6, 699–702.
- U.S. Department of Commerce (2006). *2-Minute Gridded Global Relief Data (ETOPO2v2)*, National Oceanic and Atmospheric Administration, National Geophysical Data Center.
- Weldon, R., K. Scharer, T. Fumal, and G. Biasi (2004). Wrightwood and the earthquake cycle: What a long recurrence record tells us about how faults work, *GSA Today* **14**, no. 9, 4–10.
- Wells, D. L., and K. J. Coppersmith (1994). New empirical relationships among magnitude, rupture length, rupture width, rupture area, and surface displacement, *Bull. Seismol. Soc. Am.* **84**, no. 4, 974–1002.
- Working Group on California Earthquake Probabilities (1995). Seismic hazards in southern California: Probable earthquakes, 1994 to 2024, *Bull. Seismol. Soc. Am.* **85**, no. 2, 379–439.
- Working Group on California Earthquake Probabilities (2003). Earthquake probabilities in the San Francisco bay region: 2002–2031, *U.S. Geol. Surv. Open File Rept. 03-214*.
- Zheng, G., and J. R. Rice (1998). Conditions under which velocity-weakening friction allows a self-healing versus a cracklike mode of rupture, *Bull. Seismol. Soc. Am.* **88**, no. 6, 1466–1483.

Department of Earth Sciences
University of Southern California
3651 Trousdale Parkway
Los Angeles, California 90089-0740
(G.P.E.)

Department of Geological Sciences
San Diego State University
5500 Campanile Drive
San Diego, California 92182-1020
(S.M.D.)

Scripps Institution of Oceanography
University of California, San Diego
9500 Gilman Drive
La Jolla, California 92093-0225
(J.-B.M.)

Manuscript received 7 February 2008